Receptivity of Boundary-Layer Flows over Flat and Curved Walls

by

Lars-Uve Schrader

November 2010 Technical Reports KTH Royal Institute of Technology Linné Flow Centre, KTH Mechanics SE-100 44 Stockholm, Sweden

Akademisk avhandling som med tillstånd av Kungliga Tekniska Högskolan i Stockholm framlägges till offentlig granskning för avläggande av teknologie doktorsexamen fredagen den 12 november 2010 kl 10.00 i sal F3, Kungliga Tekniska Högskolan, Lindstedtsvägen 26, Stockholm.

©Lars-Uve Schrader 2010
Universitetsservice US-AB, Stockholm 2010

Receptivity of Boundary-Layer Flows over Flat and Curved Walls

Lars-Uve Schrader

Linné Flow Centre KTH Mechanics, KTH Royal Institute of Technology SE-100 44 Stockholm, Sweden

Abstract

Direct numerical simulations of the receptivity and instability of boundary layers on flat and curved surfaces are herein reported. Various flow models are considered with the aim to capture aspects of flows over straight and swept wings such as wall curvature, pressure variations, leading-edge effects, streamline curvature and crossflow. The first model problem presented, the flow over a swept flat plate, features a crossflow inside the boundary layer. The layer is unstable to steady and traveling crossflow vortices which are nearly aligned with the free stream. Wall roughness and free-stream vortical modes efficiently excite these crossflow modes, and the associated receptivity mechanisms are linear in an environment of low-amplitude perturbations. Receptivity coefficients for roughness elements with various length scales and for free-stream vortical modes with different wavenumbers and frequencies are reported. Key to the receptivity to free-stream vorticity is the upstream excitation of streamwise streaks evolving into crossflow modes. This mechanism is also active in the presence of free-stream turbulence.

The second flow model is that of a Görtler boundary layer. This flow type forms on surfaces with concave curvature, e.g. the lower side of a turbine blade. The dominant instability, driven by a vertically varying centrifugal force, appears as pairs of steady, streamwise counter-rotating vortical rolls and streamwise streaks. The Görtler boundary layer is in particular receptive to free-stream vortical modes with zero and low frequencies. The associated mechanism builds on the excitation of upstream disturbance streaks from which the Görtler modes emerge, similar to the mechanism in swept-plate flows. The receptivity to free-stream vorticity can both be linear and nonlinear. In the presence of free-stream turbulence, nonlinear receptivity is more likely to trigger steady Görtler vortices than linear receptivity unless the frequencies of the free-stream fluctuations are very low.

The third set of simulations considers the boundary layer on a flat plate with an elliptic leading edge. This study aims to identify the effect of the leading edge on the boundary-layer receptivity to impinging free-stream vortical modes. Three types of modes with streamwise, vertical and spanwise vorticity are considered. The two former types trigger streamwise disturbance streaks while the latter type excites Tollmien-Schlichting wave packets in the shear layer. Simulations with two leading edges of different bluntness demonstrate

that the leading-edge shape hardly influences the receptivity to streamwise vortices, whereas it significantly enhances the receptivity to vertical and spanwise vortices. It is shown that the receptivity mechanism to vertical free-stream vorticity involves vortex stretching and tilting – physical processes which are clearly enhanced by blunt leading edges.

The last flow configuration studied models an infinite wing at 45 degrees sweep. This model is the least idealized with respect to applications in aerospace engineering. The set-up mimics the wind-tunnel experiments carried out by Saric and coworkers at the Arizona State University in the 1990s. The numerical method is verified by simulating the excitation of steady crossflow vortices through micron-sized roughness as realized in the experiments. Moreover, the receptivity to free-stream vortical disturbances is investigated and it is shown that the boundary layer is most receptive if the free-stream modes are closely aligned with the most unstable crossflow mode.

Descriptors

Boundary-layer receptivity, laminar-turbulent transition, swept-plate boundary layer, Görtler flow, leading-edge effects, swept-wing flow, crossflow vortices, Görtler rolls, disturbance streaks, wall roughness, free-stream turbulence

Preface

This thesis deals with the receptivity, instability and transition to turbulence in spatially developing boundary layers on flat and curved walls. These physical processes were investigated using direct numerical simulation. A brief overview over the basic concepts and numerical methods is presented in the first part. The second part is a collection of the articles listed below. Papers 1 to 4 appear here in the same form as the corresponding submitted and published versions except for some adjustments to the present thesis format and a few corrections of errata. Papers 5 and 6 are internal technical reports.

Paper 1

L.-U. Schrader, L. Brandt & D.S. Henningson, 2009 Receptivity mechanisms in three-dimensional boundary-layer flows. $J.\ Fluid\ Mech.\ 618,\ pp.\ 209–241$

Paper 2

L.-U. SCHRADER, S. AMIN & L. BRANDT, 2010

Transition to turbulence in the boundary layer over a smooth and rough swept plate exposed to free-stream turbulence. J. Fluid Mech. 646, pp. 297–325

Paper 3

L.-U. SCHRADER, L. BRANDT & T. A. ZAKI, 2010 Receptivity, instability and breakdown of Görtler flow. Submitted to J. Fluid Mech.

Paper 4

L.-U. SCHRADER, L. BRANDT, C. MAVRIPLIS & D. S. HENNINGSON, 2010 Receptivity to free-stream vorticity of flow past a flat plate with elliptic leading edge. *J. Fluid Mech.* **653**, pp. 245–271

Paper 5

L.-U. Schrader, 2010

Nonlinear receptivity of leading-edge flow to oblique free-stream vortical modes. $Internal\ report$

Paper 6

L.-U. Schrader, D. Tempelmann, L. Brandt, A. Hanifi & D. S. Henningson, 2010 Numerical study of boundary-layer receptivity on a swept wing. Internal report

Authors' contributions to the papers

The research project was initiated by Dr. Luca Brandt (LB) who is Lars-Uve Schrader's (LS) main advisor. Prof. Dan Henningson (DH) acts as the co-advisor. In 2009 LB initiated a collaboration with Prof. Tamer Zaki (TZ) from Imperial College London, UK. As a result, LS spent six months with TZ's research group.

Paper 1

The modification of the simulation code and the computations were performed by LS with feedback from LB. Most of the paper was written by LS with input from LB and DH.

Paper 2

LS carried out the implementation of the surface roughness and the adaptation of the free-stream turbulence code to three-dimensional flows. The simulations were performed by Subir Amin as a part of his Master's Thesis and by LS. Most parts of the paper were written by LS with the help of LB, who wrote the section about the breakdown.

Paper 3

LS carried out the receptivity calculations using the open-source spectral element code Nek5000 (Argonne National Laboratory, USA). TZ performed the simulations of laminar-turbulent transition due to free-stream turbulence. LS analyzed the data and wrote the manuscript with the help of TZ and LB.

Paper 4

The spectral element code Nek5000 was used. LS modified parts of the code for the handling of the computational mesh and the boundary conditions with the help of Prof. Catherine Mavriplis (CM). LS performed the computations and wrote the paper with inputs from LB, CM and DH.

Paper 5

LS carried out the simulations, using the code Nek5000, and wrote the report.

Paper 6

LS and David Tempelmann (DT) developed the computational meshes. The initial and boundary conditions were extracted from RANS simulations by Ardeshir Hanifi (AH). The simulations were performed by LS and DT, using Nek5000. The report was written by LS with inputs from LB, DT, AH and DH.

Abstract	iii
Preface	v
Part I – Introduction	1
Chapter 1. Introduction	2
1.1. Boundary layer	2
1.2. Receptivity	3
1.3. Instability	3
1.4. Breakdown to turbulence	4
Chapter 2. Boundary-layer flows	5
2.1. Characteristic scales	5
2.2. Flow over wings	6
2.3. Model problems	8
2.3.1. Swept-plate flow	8
2.3.2. Flow over concave plates	10
2.3.3. Flow past elliptic leading edges	11
2.3.4. Swept-wing flow	13
Chapter 3. Instability	15
3.1. Linearized stability equations	15
3.2. Linear stability theory	16
3.3. Two examples of modal boundary-layer instability	18
3.3.1. Crossflow instability	18
3.3.2. Görtler instability	20
3.4. Nonmodal stability theory	22
3.5. An example: Boundary-layer streaks	23
Chapter 4. Receptivity	25
4.1. Receptivity coefficients	26
4.2. Examples of boundary-layer receptivity	28
4.2.1. Direct receptivity of swept-plate flow to roughness	28
4.2.2. Receptivity to vertical vorticity at a leading edge	29
4.2.3. Nonlinear receptivity of Görtler flow to free-stream vorticity	31
Chapter 5. Breakdown	33
5.1. Examples of secondary instability and breakdown	33
5.1.1. Streak instability in flat-plate flows	33
5.1.2. Secondary instability of Görtler rolls	34

5.1.3. Turbulent spots in swept-plate flows	35
Chapter 6. Numerical methods	37
6.1. Direct numerical simulation	37
6.2. Simulation codes	38
6.3. Comparison	40
Chapter 7. Summary and outlook	42
Acknowledgements	44
Bibliography	47
Part II – Papers	51
Paper 1. Receptivity mechanisms in three-dimensional boundary layer flows	y- 55
Paper 2. Transition to turbulence in the boundary layer over a smooth and rough swept plate exposed to free- stream turbulence	97
Paper 3. Receptivity, instability and breakdown of Görtler flow	135
Paper 4. Receptivity to free-stream vorticity of flow past a flat plate with elliptic leading edge	t 183
Paper 5. Nonlinear receptivity of leading-edge flow to oblique free-stream vortical modes	219
Paper 6. Numerical study of boundary-layer receptivity on a swept wing	237

Part I Introduction

CHAPTER 1

Introduction

The present thesis reports numerical studies of the receptivity, instability and breakdown to turbulence of boundary-layer flows over flat and curved surfaces. Obviously, the notions 'boundary layer', 'receptivity', 'instability' and 'breakdown' play a central role for the current work. These are briefly introduced here and explained in more detail in §§2, 4, 3 and 5, respectively.

1.1. Boundary layer

The boundary-layer concept is closely related with the internal friction in a flow field due to the viscosity of the fluid. Already Newton described in his Principia Mathematica (1687) that the friction force per unit area (the shear stress τ) behaves as $\tau = -\mu(\mathrm{d}u/\mathrm{d}y)$ for one-dimensional flows, where μ stands for the viscosity and du/dy is the gradient of the flow velocity. Before the 20th century it was believed that τ is negligible in Newtonian fluids because of the very low viscosity of these fluids (air: $\mu \sim 10^{-5}$). This assumption led to the result that a solid body moving relative to a fluid does not experience a drag force. This is clearly against intuition, experience and experimental evidence, as already noticed by d'Alembert in the mid of the 18th century. About 150 years later the German physicist Ludwig Prandtl was able to resolve d'Alembert's paradox by introducing the concept of boundary layer (Prandtl 1905). This is a very thin fluid layer on the surface of a body in a flow, for instance a wing in an airstream (see figure 1.1a). Prandtl assumed that the fluid sticks to the wall of the body (no slip) where the flow velocity - for a fixed body - hence is zero, and that the velocity increases from zero to the value of the free stream across a very thin layer. Thus, the wall-normal component of $\nabla \mathbf{u}$ becomes large inside the boundary layer and the shear stress is relevant even in fluids with low viscosity. In particular, the shear stress at the wall exerts a drag force on the body, the skin-friction drag. The boundary-layer theory thus offered an explanation for the conventional wisdom that a body moving through a fluid experiences a force. Outside the boundary layer, where both μ and $\nabla \mathbf{u}$ are small, the flow behaves essentially as an inviscid flow.

The flow in the boundary layer may be smooth and ordered (laminar) or swirling and chaotic (turbulent). On an airplane wing, for instance, the flow starts out as laminar at the leading edge. At some location downstream of the leading edge, the laminar flow becomes unstable and turns into a turbulent motion. The boundary layer is said to undergo a laminar-turbulent transition.

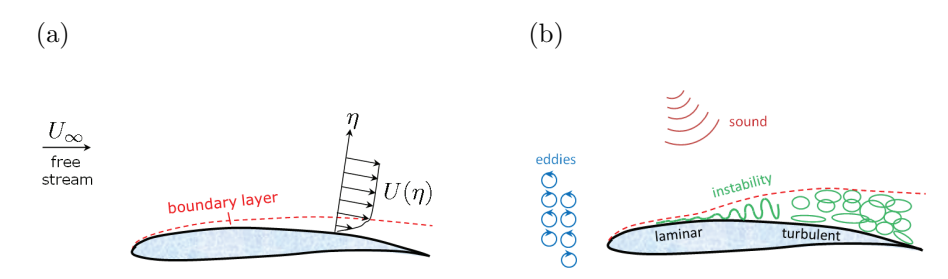


FIGURE 1.1. (a) The boundary layer on a fixed airfoil in a moving fluid (e.g. in a wind tunnel). The fluid sticks to the surface of the airfoil, and the flow velocity increases from zero to the free-stream velocity across the thin boundary layer. (b) The receptivity of the boundary layer to external perturbations, e.g. free-stream eddies or sound waves, may induce instabilities inside the boundary layer.

Being a complex process, transition does not happen suddenly but in three steps – the receptivity, the instability and the breakdown.

1.2. Receptivity

No flow in nature and engineering applications is disturbance-free. The disturbances present in the flow field may enter the boundary layer via its boundaries, which are the wing surface and the edge separating the layer from the free stream (figure 1.1a). Examples are roughness or vibrations of a wing surface and sound waves or eddies in the free stream, as sketched in figure 1.1(b). These disturbances may transfer energy to the boundary layer and establish boundary-layer instabilities which may amplify and attain amplitudes far above those of the external disturbances. The coupling between the ambient disturbances and the boundary-layer instabilities is denoted receptivity. It is obvious that the receptivity strongly depends on the perturbation environment around the boundary layer. Thus, receptivity is not a characteristic of the boundary layer alone, but of the entire flow field including the free stream and the boundaries, e.g. the surface of a wing.

1.3. Instability

Laminar boundary layers cannot be sustained under all flow conditions. Consider the flow over a wing model in a wind tunnel. The wing surface is usually imperfect and exhibits tiny irregularities. These perturb the laminar boundary layer given that the layer is receptive to the surface irregularities. The strength of these perturbations depends, among other aspects, on the speed of the airstream in the wind-tunnel test section. For low speeds the kinetic energy of the perturbations is small and fully converted into heat by the frictional forces in the boundary layer. At higher flow rates, the perturbations due to the surface imperfections become more energetic such that the energy drain by the frictional shear stresses may become insufficient. The perturbation energy

4 1. INTRODUCTION

is no longer fully removed from the boundary layer. Thus, the energy balance of the original laminar flow is disrupted and the perturbations grow in amplitude. The instabilities produced can be of modal or nonmodal type. Modal instabilities (modes) take the form of disturbance waves. The amplitudes of these modes grow or decay exponentially depending on the flow conditions. In many boundary-layer types, nonmodal instabilities may emerge in the presence of several interacting modes. The amplitude of these nonmodal disturbances does not grow exponentially, which allows for a clear distinction between modal and nonmodal instabilities. Even in the presence of boundary-layer disturbances, the fluid motion near the wing surface is still called laminar; however, the boundary-layer state is different from the original undisturbed laminar flow.

1.4. Breakdown to turbulence

The boundary-layer instabilities cannot amplify beyond all bounds, as nature does not allow for infinities. Instead, the disturbance amplitude levels out at a certain value. At this stage, the disturbance energy inside the boundary layer is tremendous and the instabilities themselves become unstable. Any additional supply of perturbation energy from the free stream over the wing may feed a new type of disturbance called secondary instability. These secondary disturbances amplify rapidly and force the boundary layer towards a new state which is more dissipative. The primary instabilities fall apart into smaller flow structures – they break down to turbulence. In the turbulent boundary layer the balance between the kinetic energy of the turbulent flow structures and the energy drain in the form of heat is reestablished.

CHAPTER 2

Boundary-layer flows

2.1. Characteristic scales

It is convenient to describe fluid flows in terms of non-dimensional variables. For this purpose, a reference length $L_{\rm ref}$ and a reference speed $U_{\rm ref}$ are introduced, chosen such that they reflect the characteristics of the flow. The scales $L_{\rm ref}$ and $U_{\rm ref}$ also define a reference time $t_{\rm ref} = L_{\rm ref}/U_{\rm ref}$. The pressure of the flow field is normalized by $\rho_{\rm ref}U_{\rm ref}^2/2$, where $\rho_{\rm ref}$ is the reference density of the fluid ¹. Finally, the fluid viscosity ν is made non-dimensional by the convective scale $U_{\rm ref}L_{\rm ref}$, which is a measure for the inertia of the flow².

Boundary-layer flows develop owing to a competition between inertial and frictional forces acting on the fluid (cf. $\S1.1$). It is therefore customary to introduce the parameter

$$Re = \frac{U_{\text{ref}}L_{\text{ref}}}{\nu},\tag{2.1}$$

the Reynolds number, called after the experimenter Osborne Reynolds (Reynolds 1883). Small values of Re indicate flows dominated by viscous forces, whereas large Reynolds numbers characterize convection-dominated flows with thin boundary layers. Common choices of $L_{\rm ref}$ and $U_{\rm ref}$ are the boundary-layer thickness δ and the free-stream speed U_{∞} , respectively. These two scales reflect in a proper manner the fastest variations of boundary-layer flows (those across the layer), which are of the order U_{∞}/δ . There exist different ways of defining the boundary-layer thickness; δ may, for instance, be taken as the distance from the wall, at which the streamwise velocity has reached 99 % of the outer flow velocity U_{∞} . This measure is called the 99 % thickness and labeled by the symbol δ_{99} . The boundary-layer thickness can also be described in terms of integral quantities. These are obtained after an integration of the streamwise velocity profile U(y) along the vertical coordinate y, starting at the wall ('0')

¹This thesis deals exclusively with incompressible flows, for which the fluid density ρ is a constant and $\rho_{\rm ref}$ is needed for dimensional reasons only.

²The symbol ν stands for the kinematic viscosity, related to the dynamic viscosity μ used in §1.1 via $\nu = \mu/\rho$.

and reaching far out into the free stream (' ∞ '),

$$\delta^* = \int_0^\infty \left(1 - \frac{U(y)}{U_\infty} \right) dy,$$

$$\theta = \int_0^\infty \frac{U(y)}{U_\infty} \left(1 - \frac{U(y)}{U_\infty} \right) dy.$$
(2.2)

The thicknesses δ^* and θ are the displacement thickness and the momentum-loss thickness of the boundary layer, respectively. These are illustrated in figure 2.1 for the example of a Blasius profile. Blasius flow is the boundary-layer flow over an infinitely thin flat plate downstream of the plate leading edge (zero pressure gradient). The displacement thickness is the distance, by which a hypothetical inviscid-flow profile must be shifted away from the wall in order to obtain the same volume flux as for the boundary-layer profile (figure 2.1a). Analogously, the momentum-loss thickness corresponds to the distance, by which an inviscid-flow profile must be shifted away from the wall in order to obtain the same transport of streamwise momentum as for the boundary-layer profile (figure 2.1b). The displacement thickness is often used to define the Reynolds number, i.e. $Re = U_{\infty} \delta^* / \nu$. In §2.3, we will also consider alternative definitions of Re.

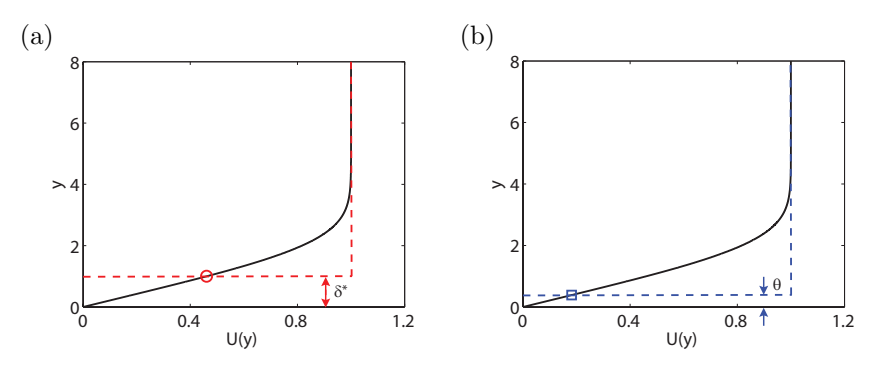


FIGURE 2.1. (a) The displacement thickness and (b) the momentum-loss thickness of a Blasius profile.

2.2. Flow over wings

Figure 2.2 sketches the flow over a straight and a swept wing. Straight wings are preferable for low-speed flight due to the beneficial lift performance at low velocities. An example of a modern aircraft with straight wings is the Bombardier Dash 8 Q400 (cruise speed 650 km/h). In contrast, high-speed airliners usually have swept wings. The sweep of the wing shifts the formation of shock waves at the wing leading edge towards speeds above those typical for cruising flight, thus avoiding an increase of resistance due to wave drag. The

Boeing 777 (cruise speed 900 km/h), with a wing sweepback of about 32°, shall serve as an example here.

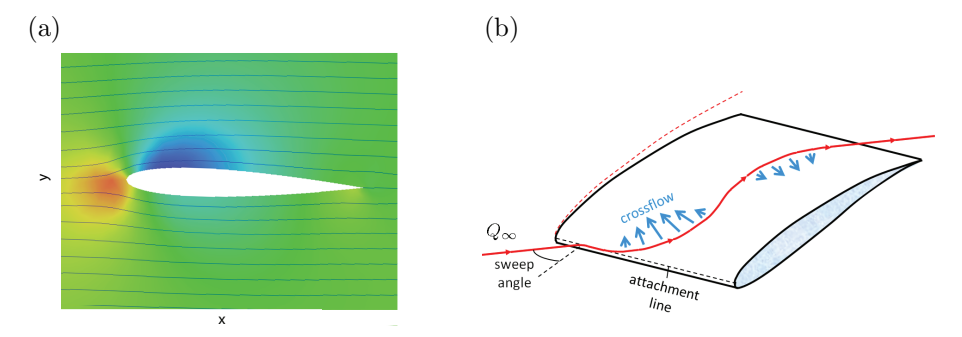


FIGURE 2.2. The features of flow over wings. (a) x-y plane of the pressure p and the streamlines around a straight wing (blue, $p < p_{\infty}$; red, $p > p_{\infty}$, with p_{∞} being the free-stream pressure). The flow is from left to right. (b) Schematic of the flow around a swept wing.

Figure 2.2(a) highlights the features of the flow field around a straight wing. The flow ahead of the leading edge separates into two streams passing the upper and the lower side of the wing. A stagnation region forms where the fluid impinges on the leading edge. In this region the pressure is significantly higher than that of the free stream. Downstream of the stagnation line, the shape of the wing redirects and accelerates the flow, causing a pressure drop in the streamwise direction. After passing its minimum value on the upper wing side, the pressure rises again towards the wing trailing edge, accompanied by a flow deceleration. The streamwise pressure and velocity gradients depend on the wing curvature and in particular on the shape of the leading edge. In figure 2.2(b) the characteristics of flow over a swept wing are depicted. Swept wings also impose chordwise pressure variations on the flow, but the pressure gradient is no longer aligned with the free stream. This leads to a deflection of the streamlines from their original orientation upstream of the wing, producing the S-shape shown in the figure. The streamline curvature is associated with a centrifugal force driving a secondary flow inside the boundary layer (see §2.3.1). This *crossflow* is of great importance for the instability of swept-wing flows.

Even with today's computer power, it is not possible to perform accurate, well-resolved simulations of flows around entire wings. Instead, researchers resort to simplified model flows, retaining certain aspects of wing flows while discarding others. The flows discussed herein are assumed to be incompressible. All flow models incorporate the assumption of a spanwise invariant mean flow, i.e. they reflect the flow over a wing with infinite span. Obviously, airplane wings have finite spans. However, in the mid-span region – far enough away from the wing tip and the fuselage – flows over infinite- and finite-span wings are essentially the same. On the other hand, flow phenomena related to the

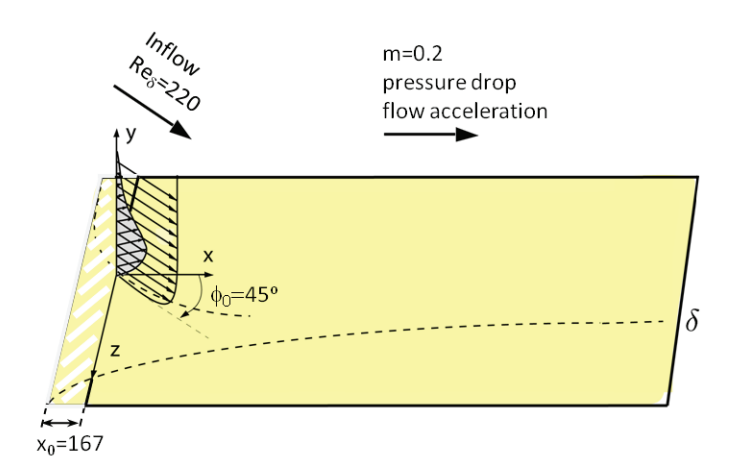


FIGURE 2.3. Schematic of the flow over a swept flat plate downstream of the leading edge.

finite wing length, e.g. the drag induced by the wing tip vortices, fall outside the assumption of spanwise invariant mean flows. In the following, the flow models considered in this thesis are presented.

2.3. Model problems

The first model problem considered is the flow over a swept flat plate (figure 2.3). The inflow boundary of the physical domain is located downstream of the leading edge, i.e. the incoming flow features a developed boundary layer with a displacement thickness δ_0^* . The incident free stream Q_{∞_0} is at an angle ϕ_0 with respect to the chord of the plate. Here, Q_{∞_0} is decomposed into the chordwise and spanwise velocities U_{∞_0} and W_{∞_0} , respectively. The quantities δ_0^* and U_{∞_0} are used here to define the inflow Reynolds number

$$Re_{\delta_0} = \frac{U_{\infty_0} \delta_0^*}{\nu}.$$
 (2.3)

The characteristic feature of swept-plate flow is the chordwise velocity variation and the presence of a spanwise velocity. Here, we impose a free stream obeying

$$U_{\infty}(x) = U_{\infty_0} \left(1 + \frac{x}{x_0} \right)^m,$$

$$W_{\infty}(x) = W_{\infty_0}, \qquad (2.4)$$

where x denotes the chordwise coordinate (x = 0 at the inflow plane) and x_0 is the chordwise distance between the virtual origin of the boundary layer ('leading edge') and the inflow plane. The exponent m determines the degree of acceleration (m > 0) or deceleration (m < 0) of the free stream. The relations

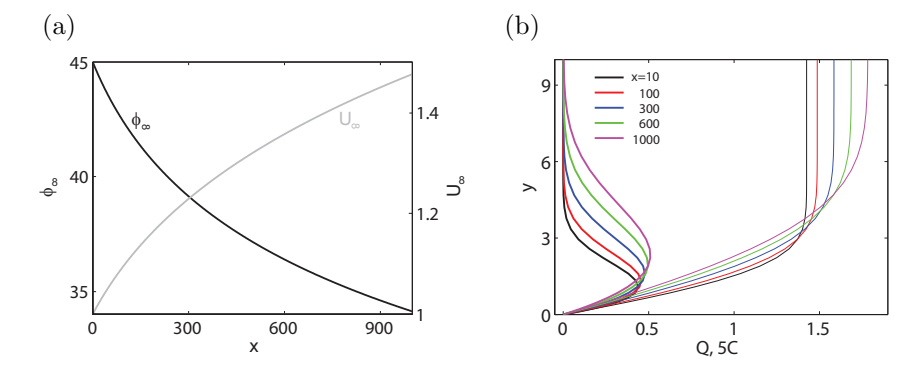


FIGURE 2.4. (a) Chordwise velocity (U_{∞}) according to (2.4) and streamline angle (ϕ_{∞}) in the free stream (y=25) versus the chordwise coordinate for m=0.2. (b) Streamwise velocity profiles (thin lines) and crossflow profiles (multiplied by 5; thick lines) at various chordwise locations.

in (2.4) are those of Falkner-Skan-Cooke flow, allowing for a self-similar solution of the mean-flow profiles (Falkner & Skan 1931; Cooke 1950). Note that the swept-plate flow is fully characterized by the values of Re_{δ_0} , ϕ_0 and m, which are given in figure 2.3. The distance x_0 follows from

$$x_0 = \frac{m+1}{2} \, \frac{Re_{\delta_0}}{c^2},\tag{2.5}$$

where c is a constant for self-similar boundary layers, which must be calculated numerically. The value of the present swept-plate flow is $c = 0.89^3$

Figure 2.4 shows some important characteristics of swept-plate flows. The chordwise acceleration of the free stream (m = 0.2) causes curved external streamlines with downstream decreasing streamline angles (figure 2.4a). The streamline curvature is associated with a centrifugal force on the fluid elements. If the flow field is decomposed into components parallel and normal to the external streamlines, the profiles Q(y) and C(y) in figure 2.4(b) are obtained. These are the streamwise and crossflow velocities, respectively. The physical explanation of the crossflow is as follows. In the free stream, the centrifugal force is counterbalanced by the pressure force. Towards the wall, the flow is retarded and the centrifugal force decreases, whereas the pressure is essentially unaffected. The resulting force imbalance induces a secondary flow in the cross-stream direction - the crossflow - which is maximum in the bulk of the boundary layer and vanishes at the layer edge. The crossflow profiles are crucial for the instability characteristics of swept-plate flows (see §3.3.1) and also play an important role in flows over swept wings. Therefore - and because of the availability of analytical baseflow profiles - swept-plate flows

³The constant c is the ratio between the displacement thickness and the Falkner-Skan length scale, $c = \delta^*(x)/\delta_{FS}(x)$. The Falkner-Skan length $\delta_{FS}(x) = \sqrt{2/(m+1)}\sqrt{\nu x/U_{\infty}}$ is used to form the similarity variable $\eta(x,y) = y/\delta_{FS}(x)$. See paper 1 for details.

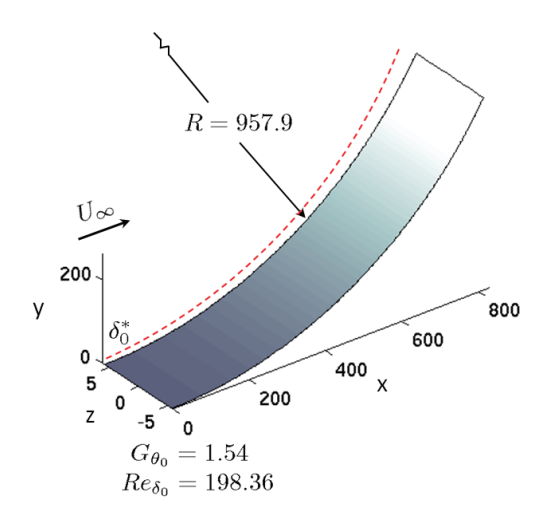


FIGURE 2.5. Schematic of the flow over a concave plate downstream of the leading edge.

of Falkner-Skan-Cooke type were extensively studied (Crouch 1993; Choudhari 1994; Högberg & Henningson 1998, for instance). On the other hand, the influences of the leading edge and of the surface curvature of swept wings are not captured within this approximation.

2.3.2. Flow over concave plates

Figure 2.5 depicts the flow over a concave plate downstream of the leading edge. The boundary layer forming on the plate is known as the Görtler boundary layer (Görtler 1941). The prominent characteristic of Görtler flows is the presence of a centrifugal force acting on the fluid in the wall-normal direction. The speed of the incoming free stream is U_{∞} , and the boundary layer features a displacement thickness of δ_0^* at the inflow plane of the physical domain. The quantities U_{∞} and δ_0^* , chosen to be the reference length and speed, are used to formulate the inflow Reynolds number

$$Re_{\delta_0} = \frac{U_{\infty_0} \delta_0^*}{\nu}.$$
 (2.6)

The flow is fully determined by Re_{δ_0} and by the radius of curvature R of the plate, which are given in figure 2.5. Görtler (1941) introduced an alternative control parameter, the Görtler number

$$G_{\theta} = \frac{U_{\infty_0} \theta}{\nu} \sqrt{\frac{\theta}{R}} = Re_{\theta} \sqrt{\frac{\theta}{R}}.$$
 (2.7)

Traditionally, the momentum-loss thickness θ rather than the displacement thickness δ^* of the Görtler boundary layer is used in the definition of the Görtler number. G_{θ} combines the Reynolds number (based on θ) with a non-dimensional curvature parameter. The flow over the concave plate is hence

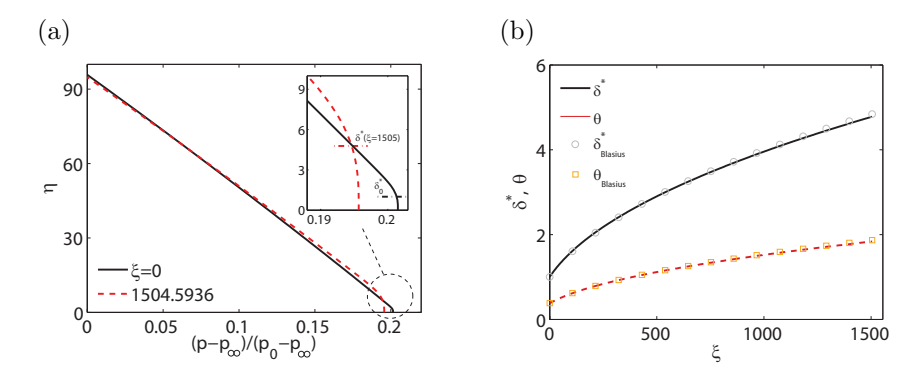


FIGURE 2.6. (a) Wall-normal pressure distribution of Görtler flow. (b) Displacement and momentum-loss thicknesses of the Görtler boundary layer as compared with the Blasius boundary layer.

fully described by one single parameter (G_{θ_0}) instead of two (Re_{δ_0}) and R, where G_{θ_0} is the inflow Görtler number

$$G_{\theta_0} = \frac{U_{\infty_0} \theta_0}{\nu} \sqrt{\frac{\theta_0}{R}},\tag{2.8}$$

with θ_0 being the inflow momentum-loss thickness. The value of G_{θ_0} considered here is given in figure 2.5.

Figure 2.6(a) shows that the vertical pressure decreases away from the concave wall. This pressure distribution is a result of the increase of the balancing centrifugal force in the wall-normal direction owing to a decrease of the radius of the streamlines. The inset of figure 2.6(a) shows that the wall-normal pressure gradient relaxes towards zero inside the boundary layer, in agreement with the vertical boundary-layer momentum equation $\partial p/\partial \eta = 0$. The streamwise development of the boundary layer (e.g. its thicknesses) is hardly affected by the presence of the wall-normal centrifugal force and essentially corresponds to that in Blasius flow (figure 2.6b). The Görtler boundary layer is a model for the flow past the concave regions of wings and blades. These regions are usually found on the lower side of the aerodynamic shape. Görtler flow is in particular relevant on turbine blades. The present model incorporates the most important aspects of these flows – the wall curvature and the resulting wall-normal centrifugal forces. Leading-edge effects are, however, excluded from our analysis.

2.3.3. Flow past elliptic leading edges

Figure 2.7 shows the third flow model considered. A flat plate with an elliptic leading edge serves as a model of a straight wing. The shape of the leading edge is that of a modified super-ellipse (MSE, Lin $et\ al.\ 1992$). In contrast to a regular ellipse, the exponent p of the MSE (see inset of figure 2.7b) is not a constant of two, but changes monotonically from two to three between the nose

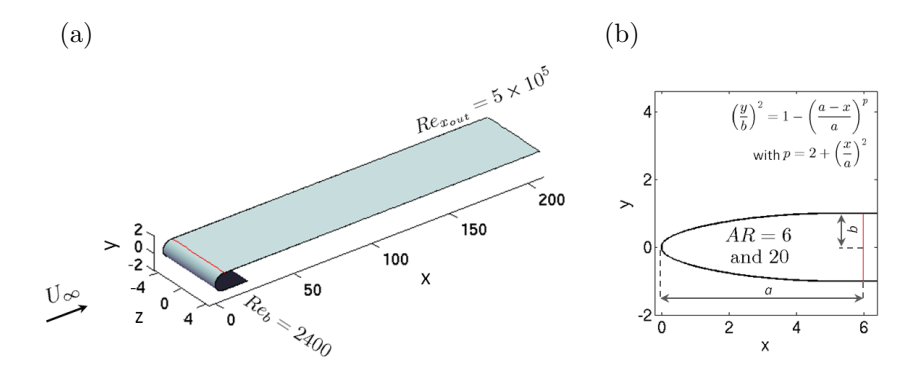


FIGURE 2.7. Schematic of the flow over a flat plate with an elliptic leading edge.

of the leading edge and the joint to the flat plate. This guarantees that not only the contour but also the slope and the curvature of the plate are smooth at the juncture. The shape of the leading edge can be altered by changing the semi-major and semi-minor ellipse axes a and b, which are related with each other via the leading-edge aspect ratio AR = a/b. A small value of AR indicates a blunt leading edge, whereas slender leading edges have a large AR. Here, the semi-minor axis b, which is also the half-thickness of the plate, shall serve as the reference length and the free stream velocity U_{∞} as the reference speed of the flow. The Reynolds number is based on these two quantities,

$$Re_b = \frac{U_{\infty}b}{\nu}. (2.9)$$

It is also common to express the Reynolds number in terms of the streamwise location x_{out} of the outflow boundary of the physical domain, i.e. $Re_{x_{out}} = U_{\infty}x_{out}/\nu$. The flow field around the plate is fully characterized by the values of Re_b (or $Re_{x_{out}}$) and AR, which are given in figure 2.7.

Figure 2.8(a) shows the streamwise pressure variations for two different plates with blunt (AR=6) and slender leading edges (AR=20). Downstream of the stagnation line $(c_p=1)$, the pressure drops rapidly, accompanied by a strong flow acceleration, and attains its minimum value ('suction peak') between the nose and the junction of the leading edge. Subsequently, the fluid passes a region of adverse pressure gradient where the flow decelerates. Farther downstream, on the flat part of the plate, the pressure relaxes towards a constant value. Figure 2.8(b) shows that downstream of the leading-edge juncture, the wall vorticity of the flows over the plates with elliptic leading edges converges with that of the Blasius boundary layer. Many relevant aspects of flows around straight wings are included in the model flow over a flat plate with an elliptic leading edge, for instance the stagnation region, the attachment line and the streamwise flow variations in the leading-edge vicinity. On the other hand, the downstream pressure distribution is different from that on a wing,

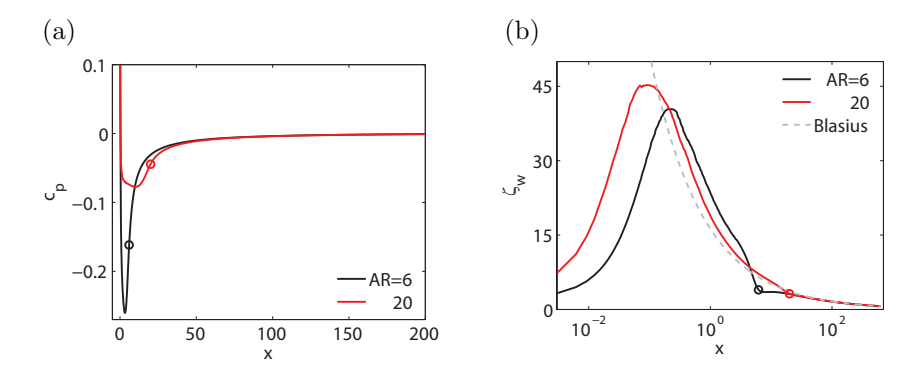


FIGURE 2.8. (a) Pressure coefficient and (b) wall vorticity in the boundary layer on a plate with elliptic leading edge. The circles mark the junction between the curved leading edge and the flat plate.

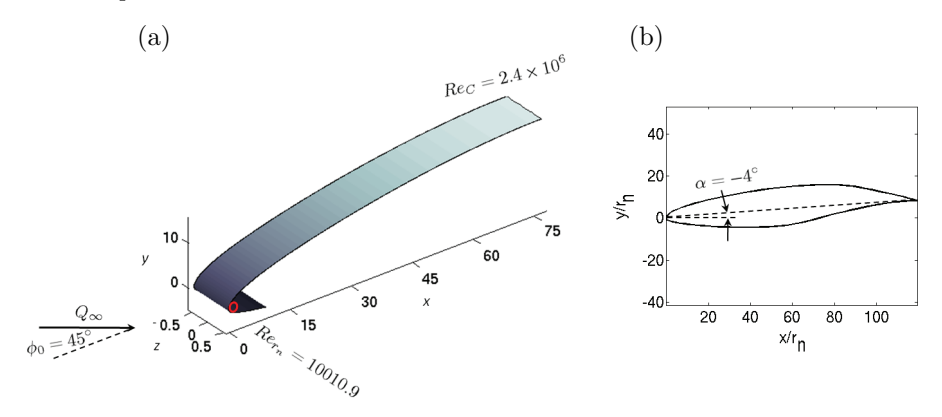


FIGURE 2.9. Schematic of the flow over a swept wing. (a) Spatial dimensions and flow parameters considered. Lengths are normalized by the nose radius (red circle). (b) The NLF(2)-0415 airfoil at an angle-of-attack of -4° .

where regions of adverse pressure gradient are usually less pronounced than for the plate model.

2.3.4. Swept-wing flow

The next configuration studied is the flow over a wing with a sweep angle ϕ_0 , as sketched in figure 2.9. The wing cross section is that of the NLF(2)-0415 airfoil (Somers & Horstmann 1985). The wing is turned at a negative angle-of-attack α . This produces a long region of accelerated flow on the upper wing side, which is desirable in order to study crossflow instability. The oncoming free stream Q_{∞} is decomposed into its chordwise and spanwise components U_{∞} and W_{∞} . We choose U_{∞} and the wing nose radius r_n to be the reference speed

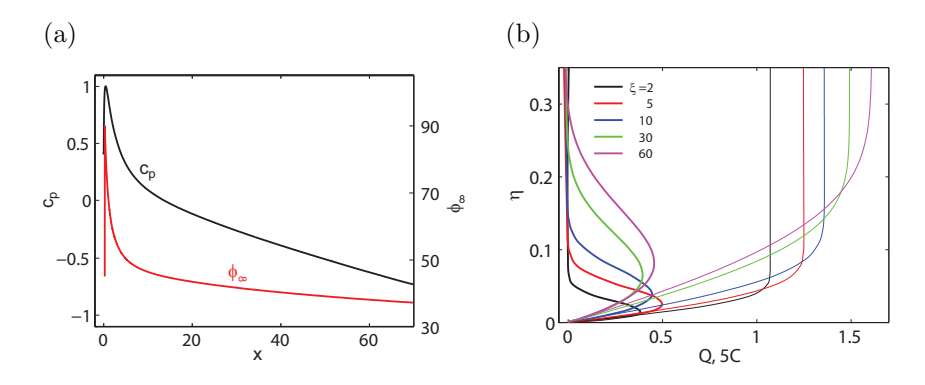


FIGURE 2.10. (a) Pressure coefficient (black) and streamline angle in the free stream for flow over a swept wing. (b) Streamwise velocity profiles (thin lines) and crossflow profiles (multiplied by 5; thick lines) at downstream locations on the wing surface.

and reference length, respectively. The Reynolds number hence is

$$Re_{r_n} = \frac{U_{\infty} r_n}{\nu}. (2.10)$$

Flows over wings are also often characterized in terms of a chord-based Reynolds number, $Re_C = Q_{\infty}C/\nu$, where C is the length of the swept wing chord. The quantities Re_{r_n} (or Re_C), ϕ_0 and α fully describe the flow conditions and are given in figure 2.9.

Figure 2.10(a) depicts the pressure distribution on the upper wing side. Downstream of the stagnation point, the pressure decreases monotonically, which gives rise to a long region of flow acceleration. Figure 2.10(a) also shows the angle of the external streamlines. The flow is incident at $\phi_0 = 45^{\circ}$. The chordwise velocity vanishes in the stagnation region such that the flow is purely spanwise when attaching to the leading edge. The subsequent chordwise acceleration becomes manifest in a monotonic decrease of the streamline angle. Downstream of the leading edge the flow behaves similar to the accelerated swept-plate flow discussed in §2.3.1. Indeed, a decomposition of the flow field into a streamwise and a cross-stream component (figure 2.10b) yields similar crossflow profiles as those shown in figure 2.4(b). The swept-wing model considered here incorporates most aspects of the flow in the mid-span region of a simple aircraft swept wing. However, we truncate the physical domain and only study the flow over the upper wing side up to a certain chordwise location. Phenomena in the trailing-edge region (e.g. flow separation) and the wake behind the wing are not considered.

CHAPTER 3

Instability

3.1. Linearized stability equations

The present study is restricted to incompressible boundary-layer flows. These flows are governed by the time-dependent incompressible Navier-Stokes equations and the continuity condition,

$$\frac{\partial \underline{\mathbf{U}}}{\partial t} + (\underline{\mathbf{U}} \cdot \nabla)\underline{\mathbf{U}} = -\nabla \underline{P} + \frac{1}{Re} \nabla^2 \underline{\mathbf{U}}, \qquad (3.1a)$$

$$\nabla \cdot \underline{\mathbf{U}} = 0. \qquad (3.1b)$$

$$\nabla \cdot \underline{\mathbf{U}} = 0. \tag{3.1b}$$

The instantaneous flow field (marked by an underline) is described by the velocity vector $\underline{\mathbf{U}}(\mathbf{x},t) = (\underline{U},\underline{V},\underline{W})$ and the pressure $\underline{P}(\mathbf{x},t)$, which both depend on space $\mathbf{x} = (x, y, z)$ and time t. The equations in (3.1) are in non-dimensional form, where velocities have been normalized by $U_{\rm ref}$ and lengths by $L_{\rm ref}$, and $Re = U_{\rm ref} L_{\rm ref} / \nu$ is the Reynolds number (cf. §2.1). The solution $\underline{\mathbf{U}}(\mathbf{x},t)$ depends on the initial state of the flow field at time t_0 ,

$$\underline{\mathbf{U}}(\mathbf{x}, t_0) = \underline{\mathbf{U}}_0, \tag{3.2}$$

and on the conditions at the boundaries of the physical domain. An example is the no-slip condition for the velocity at a solid wall.

The objective of a stability analysis is to determine the evolution of small disturbances u to the underlying baseflow U. If these disturbances grow in amplitude as time passes by (temporal perspective) or as they are advected in downstream direction (spatial perspective), the boundary layer is unstable; if they, in contrast, decay, the flow is stable. The evolution of disturbances is governed by the stability equations. These are derived by substituting the decomposition

$$\underline{\mathbf{U}} = \mathbf{U} + \varepsilon \mathbf{u},$$
 (3.3a)

$$\underline{\underline{P}} = P + \varepsilon p \tag{3.3b}$$

into (3.1), where P denotes the mean pressure and p the pressure perturbation. Within the framework of linear stability theory the disturbance amplitude ε in (3.3) is assumed to be small as compared with U_{ref} . This allows for a linearization of the stability equations, i.e. the terms of order ε^2 are discarded. After subtracting the equations of the baseflow, we obtain

$$\frac{\partial \mathbf{u}}{\partial t} + (\mathbf{U} \cdot \nabla)\mathbf{u} + (\mathbf{u} \cdot \nabla)\mathbf{U} = -\nabla p + \frac{1}{Re}\nabla^2 \mathbf{u}, \tag{3.4a}$$

$$\nabla \cdot \mathbf{u} = 0. \tag{3.4b}$$

The solution for \mathbf{u} requires the specification of an initial state, e.g. a disturbance-free flow field, and of boundary conditions, for instance an incoming disturbance at the inflow boundary of the physical domain.

3.2. Linear stability theory

If the space and time variables are separable, the boundary-layer instabilities can be assumed as time-periodic. Then, (3.3) is written as

$$\mathbf{Q}(x, y, z, t) = \mathbf{Q}(x, y, z) + \varepsilon \tilde{\mathbf{q}}(x, y, z) e^{-i\omega t}, \tag{3.5}$$

where $\underline{\mathbf{Q}} = (\underline{\mathbf{U}}, \underline{P})$ and $\mathbf{Q} = (\mathbf{U}, P)$. The disturbance takes the form of a temporal Fourier mode with an amplitude function $\tilde{\mathbf{q}} = (\tilde{\mathbf{u}}, \tilde{p})$. In classical linear theory, (3.5) is simplified by assuming a one-dimensional, locally parallel baseflow and a disturbance with an amplitude function depending on the wall-normal direction only ('normal mode'),

$$\mathbf{Q}(x, y, z, t) = \mathbf{Q}(y) + \varepsilon \tilde{\mathbf{q}}(y) e^{i(\alpha x + \beta z - \omega t)} + \text{compl. conjugate.}$$
 (3.6)

This approach was in particular successful in viscous theory based on the Orr-Sommerfeld/Squire system (Orr 1907; Sommerfeld 1908; Squire 1933). The normal-mode ansatz is valid not only in strictly parallel flows (e.g. Couette flow), but also in flows with a slow streamwise evolution. An example is the laminar flat-plate boundary layer at large enough Reynolds numbers (Blasius boundary layer). The normal modes of Blasius flow predicted by the linear theory are referred to as Tollmien-Schlichting (T-S) waves. Instabilities of T-S type were indeed observed in the wind-tunnel experiment on a flat plate by Schubauer & Skramstad (1947).

The Orr-Sommerfeld and Squire equations are derived from (3.4) by invoking the assumption of parallel flow (see Schmid & Henningson 2001). This allows for the elimination of the pressure term of the vertical momentum equation after taking the divergence of the momentum equations and the Laplacian of the vertical momentum equation. The remaining pressure terms are removed by combining the streamwise and spanwise momentum equations in order to obtain a transport equation for the wall-normal vorticity. Hence, the flow variables governed are the wall-normal velocity v and the wall-normal vorticity η . For three-dimensional boundary layers (e.g. in Falkner-Skan-Cooke flows), the Orr-Sommerfeld/Squire system takes the form

$$\frac{\partial}{\partial t} \begin{pmatrix} \tilde{v} \\ \tilde{\eta} \end{pmatrix} = \begin{pmatrix} (\mathcal{D}^2 - \alpha^2 - \beta^2)^{-1} \mathcal{L}_{OS} & 0 \\ i\alpha W' - i\beta U' & \mathcal{L}_{Sq} \end{pmatrix} \begin{pmatrix} \tilde{v} \\ \tilde{\eta} \end{pmatrix}, \tag{3.7}$$

where the tilde indicates a Fourier transformation to wavenumber space. The linear Orr-Sommerfeld and Squire operators \mathcal{L}_{OS} and \mathcal{L}_{Sq} are

$$\mathcal{L}_{OS} = (-i\alpha U - i\beta W)(\mathcal{D}^2 - \alpha^2 - \beta^2) + i\alpha U'' + i\beta W''$$

$$+ \frac{1}{Re}(\mathcal{D}^2 - \alpha^2 - \beta^2)^2,$$
(3.8a)

$$\mathcal{L}_{Sq} = -i\alpha U - i\beta W + \frac{1}{Re}(\mathcal{D}^2 - \alpha^2 - \beta^2). \tag{3.8b}$$

The quantities α and β are the streamwise and spanwise wavenumbers, respectively, and \mathcal{D} stands for the derivative operator in wall-normal direction. The prime and double prime denote the first and second derivatives of the parallel baseflow. The system (3.7) is an initial-value problem with the solution

$$\tilde{q} = e^{\mathcal{L}t} \tilde{q}|_{t=t_0},\tag{3.9}$$

where $\tilde{q} = (\tilde{v}, \tilde{\eta})$, and \mathcal{L} labels the matrix operator of (3.7). Key to a stability analysis are the eigenvalues σ_i and the eigenfunctions ϕ_i of the matrix exponential

$$e^{\mathcal{L}t}\phi_i = \sigma_i\phi_i, \qquad |\sigma_1| > \dots > |\sigma_n|.$$
 (3.10)

The instability condition stated in $\S 3.1$ can now be mathematically formulated:

Asymptotically unstable flow, if
$$|\sigma_1| > 1$$
, (3.11a)

The eigenvalues λ_i of of the matrix operator \mathcal{L} are related with those of $e^{\mathcal{L}t}$ via $\lambda_i = \frac{1}{t}\log\sigma_i$. The values of λ_i are a measure for the temporal amplification or decay rates of the eigenmodes ϕ_i . The conditions (3.11) indicate that one eigenvalue alone governs the modal instability of the basic state, namely that pertaining to the least stable eigenmode. The value of $|\sigma_1|$ determines whether the least stable mode grows beyond all bounds or decays to zero as time $t \to \infty$, i.e. it characterizes the asymptotic temporal stability of the baseflow.

In convection-dominated flows, the *spatial* stability is often more relevant. The spatial Orr-Sommerfeld/Sqire problem is formulated by re-ordering the terms of (3.7),

$$\mathbf{0} = \begin{pmatrix} L_{OS} & 0\\ i\beta U' - i\alpha W' & L_{Sq} \end{pmatrix} \begin{pmatrix} \tilde{v}\\ \tilde{\eta} \end{pmatrix}, \tag{3.12}$$

where L_{OS} and L_{Sq} are the spatial Orr-Sommerfeld and Squire operators

$$L_{OS} = (i\omega - i\alpha U - i\beta W)(\mathcal{D}^2 - \alpha^2 - \beta^2) + i\alpha U'' + i\beta W'' \quad (3.13a)$$
$$+ \frac{1}{Re}(\mathcal{D}^2 - \alpha^2 - \beta^2)^2,$$

$$L_{Sq} = i\omega - i\alpha U - i\beta W + \frac{1}{Re}(\mathcal{D}^2 - \alpha^2 - \beta^2)$$
 (3.13b)

and ω is the angular frequency. The spatial stability of the basic state is characterized by the spatial eigenvalues of the operator matrix in (3.12), which

are the complex streamwise wavenumbers α . The spatial instability conditions are formulated with respect to the imaginary part of α

Convectively unstable flow, if
$$Im\{\alpha_1\} < 0$$
, (3.14a)

where α_1 is the eigenvalue with the smallest imaginary part. The attribute 'convective' in (3.14) indicates the streamwise nature of the modal evolution¹. The value of $\text{Im}\{\alpha_1\}$ plays the role of the spatial decay rate of the least stable mode, with negative values indicating streamwise exponential growth.

Predictions from classical linear stability theory prove inaccurate when 'non-parallel effects' become important. This is, for instance, the case for the flow field near a leading edge where the boundary layer rapidly grows in thickness and cannot be assumed as locally parallel. A successful effort to cope with flows with more than one inhomogeneous direction was the development of the method of parabolized stability equations (PSE) by Herbert & Bertolotti (1987) (see also Herbert 1997). In the PSE framework, the profiles of the boundary-layer disturbance are still locally one-dimensional, but the baseflow and the modal instability are allowed to develop moderately in the other two directions². Since the stability equations are parabolic, their solution can be obtained by an efficient spatial marching technique. Therefore, the PSE approach is ideally suited for parametric studies of boundary-layer stability. An alternative attempt to generalize the classical stability analysis is the theory of global modes (see e.g. Theofilis et al. 2002; Henningson & Åkervik 2008; Mack et al. 2008), which is based on the eigenmode ansatz

$$\mathbf{Q}(x, y, z, t) = \mathbf{Q}(x, y) + \varepsilon \tilde{\mathbf{q}}(x, y) e^{i(\beta z - \omega t)} + \text{compl. conjugate.}$$
(3.15)

The shape functions of the global eigenmodes are dependent on two spatial directions, whereas the dependence on the third direction and on time is captured by the periodic wave function. The global-mode approach is therefore appropriate in order to investigate the global stability of spanwise periodic flows.

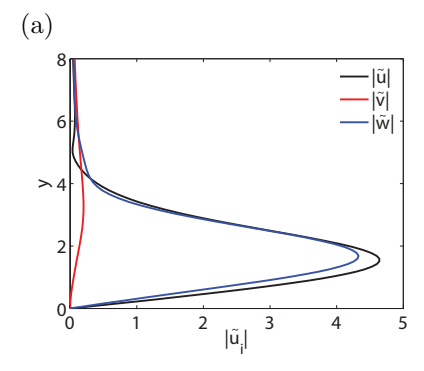
3.3. Two examples of modal boundary-layer instability

3.3.1. Crossflow instability

A spatial linear stability analysis of the Falkner-Skan-Cooke boundary layer reveals that there exist eigenvalues with $\text{Im}\{\alpha\} < 0$ for $Re_{\delta^*} = 220$. Hence, the swept-plate boundary layer discussed in §2.3.1 is linearly unstable. Figure 3.1(a) depicts the wall-normal structure of the eigenmode with frequency $\omega = 0$ and spanwise wavenumber $\beta = -0.190$. The associated spatial eigenvalue is $\alpha = 0.168 + 0.001$ i, where the real part plays the role of the streamwise

 $^{^1}$ The boundary-layer flows studied are convectively unstable. Absolute instabilities (see e.g. Schmid & Henningson 2001) are not discussed here.

²The PSE are usually applied to spanwise periodic flows, which only develop in the streamwise direction.



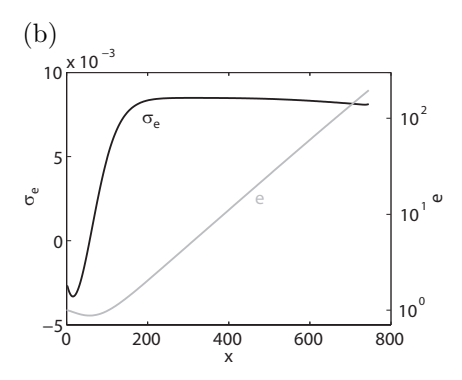


FIGURE 3.1. (a) Eigenmode with $\omega = 0$ and $\beta = -0.19$ of the Falkner-Skan-Cooke boundary layer with $Re_{\delta^*} = 220$. (b) Amplitude and growth rate of the disturbance energy obtained from a direct numerical simulation (DNS, linearized equations) of swept-plate flow with $Re_{\delta^*} = 220$. In the framework of linear stability theory, the energy growth rate is $\sigma_{\text{e.LST}} = -2\text{Im}\{\alpha\}$.

wavenumber and the imaginary part that of the streamwise decay rate. Hence, this particular mode is damped under the inflow conditions $(Re_{\delta^*} = 220)$ while becoming linearly unstable farther downstream $(Re_{\delta^*} = 253)$. This mode is chosen here because it is globally dominant in the present swept-plate boundary layer. Figure 3.1(b) depicts the streamwise evolution of the modal amplitude and of the growth rate for the disturbance energy. Since the wave vector $(Re\{\alpha\},\beta)$ points in the direction of the crossflow, the mode is referred to as a crossflow mode. Figure 3.2 shows the spatial structure of the crossflow mode. Note that the streamwise and spanwise velocity components are one order of magnitude larger than the wall-normal component. A projection of the mode onto a streamwise aligned coordinate system reveals that the disturbance takes the form of a streamwise vortex. Therefore, crossflow modes are often referred to as crossflow vortices.

The mechanism of the crossflow instabilities is closely related with the crossflow profiles of the basic state (cf. figure 2.4b). These profiles exhibit an inflection point between their maximum and the boundary-layer edge. Based on the paper by Rayleigh (1880), Fjørtoft (1950) demonstrated that a necessary condition for the instability of inflectional profiles is $C''(y)[C(y) - C(y_{ip})] < 0$ at some location in the flow, where C(y) and C''(y) stand for the present crossflow profiles and their wall-normal second derivative, respectively, and the inflection point is located at y_{ip} ($C''(y_{ip}) = 0$). Indeed, the crossflow profiles exhibit regions where Fjørtoft's criterion is fulfilled, indicating that the swept-plate boundary layer is potentially unstable. The associated instability is called inflectional – or inviscid, because the instability mechanism is not related to the viscosity of the fluid. The viscosity has, however, a stabilizing effect on the mechanism. The physical explanation of inviscid instability is based on the

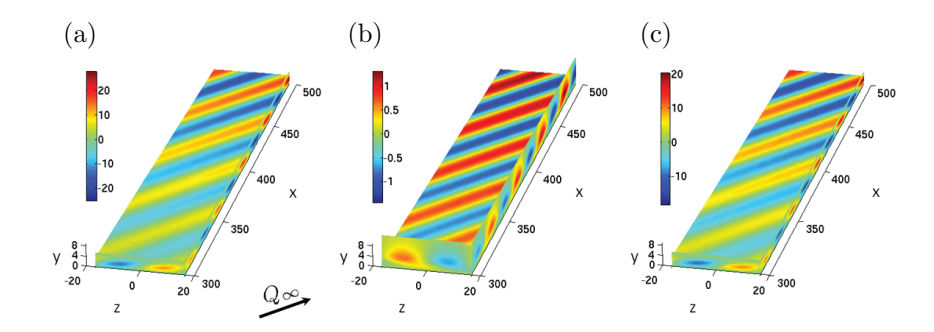


FIGURE 3.2. Spatial evolution of a steady crossflow mode ($\beta = -0.19$) in a swept-plate boundary layer ($Re_{\delta^*} = 220$) as obtained from direct numerical simulation (DNS). (a) Streamwise, (b) wall-normal and (c) spanwise disturbance velocity.

dynamics of vorticity perturbations in the vicinity of the inflection point (Lin 1955).

3.3.2. Görtler instability

The linear instability of boundary-layer flows over concave plates was first examined by Görtler (1941). Görtler boundary layers become linearly unstable for Görtler numbers above $G_{\theta} = 0.4638$ (Floryan & Saric 1982)³. The inflow Görtler number of the concave-plate flow considered in §2.3.2 is $G_{\theta_0} = 1.54$, i.e. the flow is expected to be unstable. Figure 3.3(a) shows the streamwise evolution of the mode with frequency $\omega = 0$ and spanwise wavenumber $\beta = 0.546$ in terms of the r.m.s. of the streamwise disturbance velocity. Apart from the concave plate sketched in figure 2.5, two additional plates with twice and four times as large radius of curvature are considered in the figure. While being stable at the inflow plane, the disturbances exhibit the exponential amplification typical of modal instabilities farther downstream. When plotted versus the local Görtler number the curves pertaining to the three plates collapse, which highlights the role of the Görtler number as the governing stability parameter in Görtler flows. In figure 3.4, the spatial appearance of the steady Görtler mode with $\beta = 0.546$ is shown. The mode consists of long streamwise structures of positive and negative streamwise velocity (figure 3.4a) caused by counter-rotating streamwise vortices (figures 3.4b and 3.4c). Because of this vortical motion, these modes are also called Görtler vortices or rolls.

The physical mechanism of the Görtler instability is associated with the wall-normal centrifugal force in concave-plate flows. Like the crossflow instability, the centrifugal instability is of the inviscid type, while the fluid viscosity

³The instability of Görtler boundary layers depends on the inflow conditions owing to transient behavior (Hall 1983). Classic linear stability results are therefore ambiguous for small values of G_{θ} , and hence the concept of critical Görtler number is not well-defined. The number given by Floryan & Saric (1982) should be understood as an approximate value.

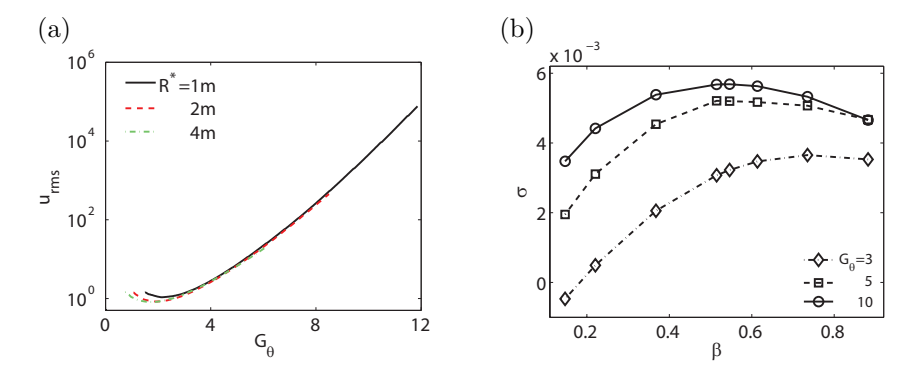


FIGURE 3.3. (a) Streamwise evolution (r.m.s. of streamwise velocity) of the steady Görtler mode with $\beta=0.546$ in flows over concave plates with three different radii of curvature. (b) Spatial growth rates of the streamwise disturbance velocity of Görtler modes with different spanwise wavenumbers at three streamwise locations.

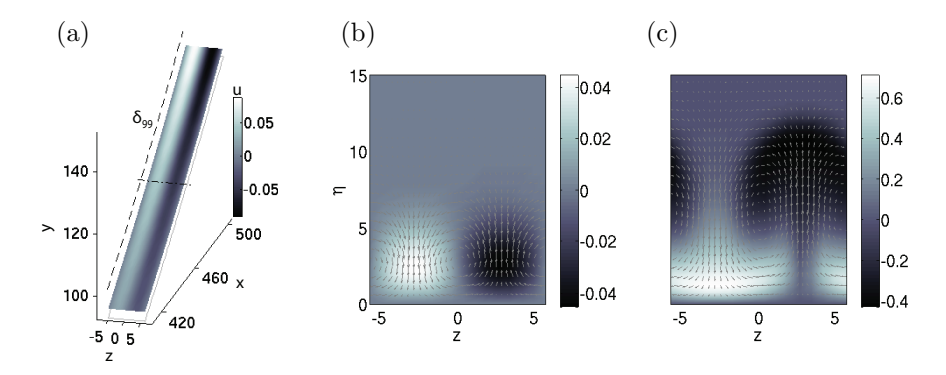


FIGURE 3.4. The structure of the steady Görtler mode with $\beta=0.546$. (a) Streamwise disturbance velocity giving rise to streaks. (b) and (c) Görtler vortices and streamwise streaks at two downstream locations.

has a stabilizing effect. Rayleigh (1916) developed a necessary and sufficient criterion (in inviscid flow) of instability known as the circulation criterion. Its simplified form (see e.g. Saric 1994) states that the baseflow profile U(r) is unstable if d|rU(r)|/dr < 0 anywhere in the flow, with r being a radial coordinate pointing towards the plate. This criterion is indeed fulfilled for the basic state on a concave plate, which is essentially of Blasius type (cf. §2.3.2). The Görtler instability is physically explained by the inability of the pressure to act as a restoring force when fluid is vertically displaced into regions of larger or smaller centrifugal forces.

3.4. Nonmodal stability theory

The wind-tunnel experiment by Schubauer & Skramstad (1947) gave strong support to the linear stability theory, which was apparently able to predict the instability of flat-plate boundary layers. However, already the work by Taylor (1939) had cast a shadow on the classical approach. Later research efforts revealed that an eigenmode analysis fails to predict the response of the Blasius boundary layer to free-stream turbulence. Klebanoff (1971) observed boundary-layer disturbances in a wind-tunnel experiment which differed severely from the T-S waves predicted by a linear eigenmode analysis. These disturbances occurred farther upstream, had a different shape and exhibited a non-exponential amplification rate. Since these instabilities are not associated with a single eigenmode of the baseflow, they are called nonmodal instabilities. The historical term 'Klebanoff modes' for these disturbances was coined before their nonmodal nature was fully understood. The development of the nonmodal stability theory started with the paper by Ellingsen & Palm (1975) who demonstrated for inviscid shear layers that there exist initial disturbances growing linearly instead of exponentially in time. These disturbances were found to produce a streaky pattern of alternating high and low streamwise velocities. The amplification of the streaks was termed 'transient growth' by Hultgren & Gustavsson (1981). Transient growth was shown to occur also in viscous flows.

The mathematical framework for transient growth was given by Butler & Farrell (1992); Reddy & Henningson (1993); Trefethen *et al.* (1993) (see also Schmid & Henningson 2001). It is based on the non-normality of the linear Navier-Stokes operator in shear flows (or of the Orr-Sommerfeld/Squire operator discussed in §3). An operator \mathcal{L} is non-normal if $\mathcal{LL}^* \neq \mathcal{L}^* \mathcal{L}$, where the star denotes the adjoint operator⁴. The transient growth of an initial disturbance at time $t = t_0$ is given by

$$G(t) = \|e^{\mathcal{L}t}\tilde{q}|_{t=t_0}\|^2. \tag{3.16}$$

The condition for nonmodal instability is formulated by means of the singular values σ_i , which are the eigenvalues of the matrix $e^{\mathcal{L}^*t}e^{\mathcal{L}t}$,

$$e^{\mathcal{L}^* t} e^{\mathcal{L} t} \phi_i = \sigma_i \phi_i, \qquad \sigma_1 \ge \dots \ge \sigma_n \ge 0.$$
 (3.17)

The condition for transient growth is stated as

Transient growth, if
$$\sigma_1 > 1$$
, (3.18a)

Transient amplification describes the short-time behavior of the boundary-layer disturbances. In contrast, the linear growth is approached when $t \to \infty$, as reflected by the attribute 'asymptotic' in (3.11). The instabilities undergoing transient growth are nonmodal, because the underlying mechanism does not

⁴The adjoint operator is implicitly defined as the operator \mathcal{L}^* fulfilling $\langle \mathcal{L}x, y \rangle = \langle x, \mathcal{L}^*y \rangle$, where $x, y \in H$ (Hilbert space) and $\langle \cdot \rangle$ is an inner product defined on H.

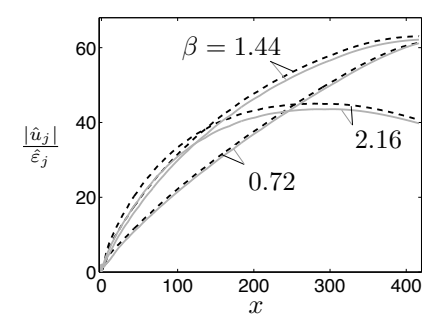


FIGURE 3.5. Streamwise amplification of steady boundary-layer streaks with different spanwise wavenumbers in the flow over a plate with an elliptic leading edge. Leading edges with aspect ratio AR = 6 (dashed lines) and AR = 20 (solid lines) are considered.

rely on the evolution of a single growing eigenmode. Instead, a linear interaction between eigenmodes of Orr-Sommerfeld and Squire type gives rise to the nonmodal instability. This results in a boundary-layer disturbance changing its shape as individual modes grow or decay in time and space at different rates. Transient growth may for this reason occur before the subsequent exponential behavior and trigger the laminar-turbulent transition prior to the asymptotic instability. The 'natural transition mechanism' due to the most unstable eigenmode is then 'bypassed', and the transition route is called *bypass transition*.

3.5. An example: Boundary-layer streaks

Consider the boundary layer on the flat plate with an elliptic leading edge introduced in §2.3.3. When exposed to a free stream with vortical disturbances, this type of flow can develop nonmodal instabilities. Figure 3.5 shows the streamwise evolution of nonmodal disturbances with frequency $\omega = 0$ and three different spanwise wavenumbers. Obviously, these instabilities do not amplify exponentially in the downstream direction, which distinguishes them from the boundary-layer eigenmodes discussed in §3.3. Eventually, the nonmodal disturbances decay (cf. figure 3.5, $\beta = 2.16$), i.e. their amplification is limited in space and time. Therefore, the evolution of nonmodal instabilities is referred to as transient (short-term) growth, as opposed to the asymptotic (long-term) behavior of the unstable eigenmodes of the flow. Figure 3.5 indicates that the transient growth rate is substantial near the leading edge and that the amplitude of the nonmodal instabilities can exceed the amplitude of their source (the free-stream disturbance here) by orders of magnitude. Therefore, nonmodal disturbances may cause a transition to turbulence before the modal instabilities (T-S waves in this case) attain significant amplitudes. Figure 3.6 illustrates the spatial appearance of the nonmodal instabilities. Most of the disturbance energy is concentrated in the streamwise velocity component (figure 3.6a). The disturbance structures are elongated in the streamwise direction

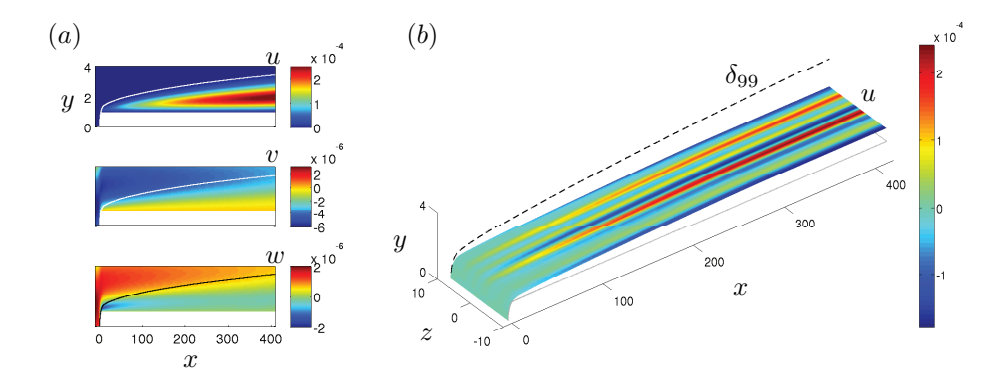


FIGURE 3.6. Streaks in the boundary layer on a flat plate with elliptic leading edge (aspect ratio AR = 6). (a) Instantaneous streamwise, vertical and spanwise disturbance velocities u, v and w in the x-y plane where u is maximum. The lines mark δ_{99} . (b) Spanwise plane of u along the wall-normal maximum of u_{rms} . Several streaks with different spanwise wavenumbers are shown.

and feature positive and negative streamwise disturbance velocities alternating in the spanwise direction (figure 3.6b). Because of their appearance, these steady disturbances are called boundary-layer streaks. Streaks were observed in a number of wind-tunnel experiments ('Klebanoff modes') long before the advent of the theory of nonmodal instability and transient growth.

A physical explanation of the nonmodal instability mechanism was proposed by Landahl (1980). It builds on the wall-normal displacement of fluid particles in shear flows by weak pairs of counter-rotating streamwise vortices ('lift-up mechanism'). These vortices originate in the free stream and penetrate into the shear layer. By promoting a vertical exchange of low-momentum fluid and high-momentum fluid, the streamwise vortices give rise to high-speed streaks in the low-momentum region near the wall and low-speed streaks in the high-momentum region near the boundary-layer edge.

CHAPTER 4

Receptivity

Boundary-layer instabilities emerge as a result of a forcing of the layer by its environment¹. Sources of such a forcing are, for example, the vortical fluctuations of a free stream or the roughness of a wall. If the forced boundary-layer disturbance is able to feed the eigenmodes of the layer with energy and modal or nonmodal instabilities arise, the layer is said to be *receptive* to the forcing.

The simplest receptivity mechanism is that of direct receptivity. Direct receptivity requires a resonance between the frequencies and wavenumbers of the enforced disturbances and those of the boundary-layer eigenmodes. A sweptplate boundary layer, for instance, is directly receptive to natural wall roughness, because the roughness exhibits a broad range of length scales – among them those of the steady crossflow modes. However, many natural free-stream disturbance sources are not 'wavenumber resonant' with the boundary-layer modes. The mismatch in wavenumber arises because the length scales of the free-stream disturbances are governed by the inviscid dynamics of the outer flow, whereas those of the eigenmodes are determined by the viscous effects inside the boundary layer. An example is the Blasius boundary layer exposed to a free-stream sound wave at a low Mach number. In the incompressible limit, the streamwise wavenumber of the acoustic wave is zero and so is the wavenumber of the disturbance enforced inside the layer (Stokes wave). Thus, the Stokes wave does not directly couple to the large-wavenumber T-S mode of the Blasius boundary layer.

Despite the lack of a direct receptivity mechanism, Blasius flow was found to be receptive to free-stream sound under certain conditions. Goldstein (1983) and Ruban (1985) proposed an explanation for this apparent contradiction by introducing the concept of length-scale conversion. For the example of Blasius flow with free-stream sound, a second – steady – source is required in order to provide the T-S wavenumber. Therefore, the receptivity mechanism is sometimes called indirect receptivity. Goldstein (1983) demonstrated by an asymptotic analysis that the rapidly developing boundary-layer region near a leading edge can convert the length scale of the enforced Stokes solution into that of the T-S wave. This is shown in figure 4.1 for the case of free-stream vorticity. Although the free-stream wave exhibits a longer wavelength than the T-S mode, the boundary layer is receptive to the free-stream disturbance. As

 $^{^1}$ In absolutely unstable flows, the instabilities are sustained without an external forcing (e.g. Schmid & Henningson 2001).

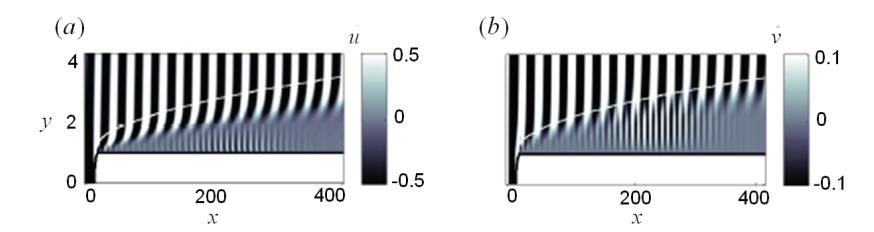


FIGURE 4.1. Excitation by free-stream vorticity of a T-S wave inside the boundary layer on a plate with an elliptic leading edge.
(a) Streamwise and (b) vertical disturbance velocities.

demonstrated by Goldstein (1985), a streamwise variation in surface geometry, e.g. a roughness bump or a suction hole, can also promote the length-scale conversion. The asymptotic theory considered by Goldstein (1983, 1985) and Ruban (1985) is based on an expansion of the disturbance in powers of 1/Re, which leads to the linearized triple-deck equations. These govern the disturbance evolution in the limit of high Reynolds numbers. The triple-deck formulation is only valid at the first neutral point of the unstable mode (branch I). A successful attempt to extend the receptivity analysis to finite Reynolds numbers and to the regions away from the first branch of instability was the finite Reynolds-number theory (FRNT) first proposed by Zavol'skii et al. (1983). The FRNT relies on the same ideas as the classical linear stability theory (see §3.2). These are the assumption of a locally parallel baseflow and the limitation to small disturbance amplitudes, allowing for a linearization of the governing equations. The FRNT was successfully applied to two-dimensional flat-plate flows (Crouch 1992; Choudhari & Streett 1992) and to Falkner-Skan-Cooke boundary layers (Crouch 1993, 1994; Choudhari 1994).

4.1. Receptivity coefficients

During the receptivity phase, the external forcing imposes the upstream amplitude ('initial condition') of the boundary-layer instabilities at the receptivity site (e.g. a roughness bump). This amplitude may therefore be called receptivity amplitude (denoted by A_R here). It is obvious that the receptivity amplitude depends on the amplitude ε of the ambient perturbation. If A_R is proportional to ε , the receptivity to the forcing is linear. It is customary to introduce the ratio between A_R and ε , referred to as receptivity coefficient,

$$C_R = \frac{A_R}{\varepsilon}. (4.1)$$

For linear receptivity, C_R is constant upon varying the forcing amplitude ε . The assumption of linear receptivity only holds for ambient perturbations with small amplitudes. The receptivity of swept-plate flow to shallow localized roughness bumps is an example for a linear mechanism. For indirect receptivity, i.e. the receptivity to a combination of two external sources (e.g. coupling of sound at

roughness), C_R is written as

$$C_R = \frac{A_R}{\varepsilon_1 \varepsilon_2},\tag{4.2}$$

where ε_1 and ε_2 are the amplitudes of the two sources. The indirect receptivity is linear if A_R is proportional to both ε_1 and ε_2 . There also exist receptivity mechanisms which are nonlinear even for small amplitudes. For example, the receptivity of boundary layers to pairs of oblique vortical free-stream waves is quadratic in the amplitude of the free-stream disturbance. The receptivity coefficient for quadratic receptivity is

$$C_R = \frac{A_R}{\varepsilon^2}. (4.3)$$

In general, we may summarize (4.1), (4.2) and (4.3) by stating

$$C_R = \frac{\text{Initial instability amplitude}}{\text{Amplitudes of the perturbation sources}},$$
 (4.4)

i.e. the receptivity coefficient is a measure for the efficiency of the energy transfer from the forcing to the boundary-layer instability. The receptivity amplitude A_R and the forcing amplitude ε should be chosen such that they reflect in a proper way the nature of the triggered instability and the characteristics of the forcing. Common choices of A_R are the wall-normal maximum of the streamwise disturbance-velocity amplitude (or the r.m.s.) and quantities based on a wall-normal integration of the disturbance-velocity profiles. The choice of ε depends on the type of disturbance source considered. An example for surface roughness is given in §4.2.1.

The receptivity coefficients are key to a receptivity analysis of boundary-layer flows. They can be combined with standard transition-prediction methods based on linear stability theory (e.g. the e^N -method) in order to provide a refined prediction tool for industrial use, including the receptivity. Since the instability amplitudes obtained by the e^N -method are usually normalized by their magnitude at the first neutral instability point, it is more convenient to define the receptivity coefficients at branch I rather than at the receptivity site. These branch-I coefficients are sometimes referred to as effective coefficients, denoted by $C_R^{\rm eff}$ here. The effective receptivity coefficients can be used to determine the disturbance amplitude A(x) at any location in the linear regime downstream of the receptivity site. If the N-factor of the instability is known, the disturbance amplitude can be written as

$$A(x) = \varepsilon C_R^{\text{eff}} e^{N(x)}. \tag{4.5}$$

Since the receptivity mechanisms depend on a wealth of factors – e.g. the flow configuration, the perturbation environment and the nature of the dominant instabilities – the application of the results from a receptivity analysis in an industrial context will require a vast database of receptivity coefficients. This motivates the continuation of receptivity research in order to develop refined theoretical receptivity models. Direct numerical simulations and large-eddy

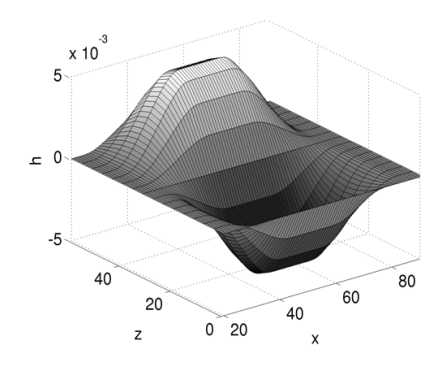


FIGURE 4.2. Streamwise localized roughness element with spanwise sinusoidal shape.

simulations like those presented in this thesis will continue to serve as validation tools for these models.

4.2. Examples of boundary-layer receptivity

4.2.1. Direct receptivity of swept-plate flow to roughness

Consider the swept-plate boundary layer depicted in figure 2.3, which is unstable to crossflow modes (§3.3.1). Steady crossflow vortices can be excited by wall roughness via a direct receptivity mechanism. This receptivity was examined here by considering the roughness element sketched in figure 4.2. The roughness is localized in the chordwise direction and periodic in the spanwise direction. Therefore, the bump enforces a steady boundary-layer disturbance with a large number of chordwise wavenumbers (denoted by α) and one single spanwise wavenumber (β_r). Instead of prescribing the roughness as a deformation of the wall, we modeled it in terms of inhomogeneous boundary conditions for the enforced disturbance. These conditions are obtained by a projection of the no-slip conditions at the bump contour onto the smooth wall (index '0'), using the wall-normal gradient of the baseflow profiles,

$$\mathbf{u}_0(x,z) = -h(x) \left(\frac{\partial \mathbf{U}}{\partial y}\right)_0 \sin(\beta_r z), \tag{4.6}$$

where h(x) is the chordwise shape of the roughness. After a chordwise Fourier transformation, the roughness model becomes

$$\tilde{\mathbf{u}}_0(\alpha, \beta_r) = -\tilde{H}(\alpha) \left(\frac{\partial \mathbf{U}}{\partial y}\right)_0 \sin(\beta_r z),\tag{4.7}$$

with $\tilde{H}(\alpha)$ being the chordwise wavenumber spectrum of the roughness. Here, the spectrum was manipulated by altering the chordwise bump shape. This is seen in figure 4.3(a), where three different bump contours (inset) and their wavenumber spectra $|\tilde{H}|$ are depicted. We also varied the spanwise wavenumber

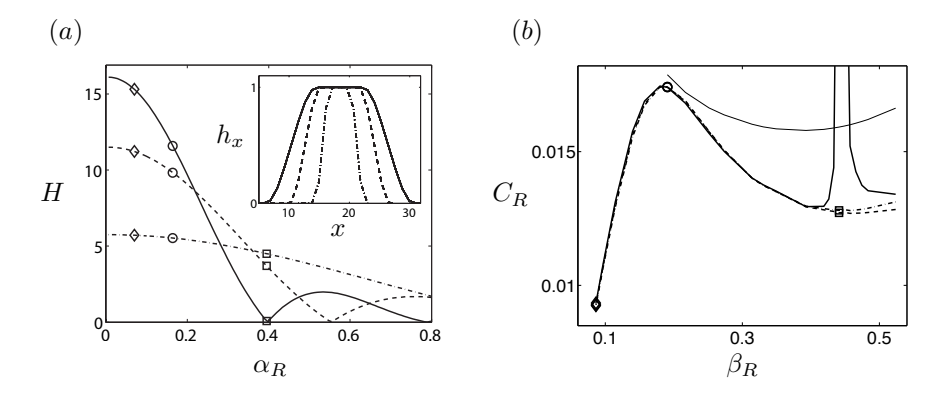


FIGURE 4.3. (a) Bumps with three different streamwise shapes in physical space (inset) and Fourier space. (b) Receptivity coefficients for roughness elements with different spanwise wavenumbers and streamwise shapes. The coefficients were extracted from DNS data. The peak is explained in paper 1. The thin curve pertains to the receptivity of a streamwise constant ('parallel') basic state.

 β_r of the roughness. The symbols in figure 4.3(a) mark the spectral bump amplitudes $|\tilde{H}(\alpha_{CF})|$ obtained at the wavenumbers α_{CF} of the unstable crossflow modes pertaining to three values of β_r . Figure 4.3(b) shows the receptivity coefficients obtained. The most remarkable result is that the receptivity becomes independent of the chordwise bump shape for nearly all spanwise wavenumbers considered². This shape independence is obtained if the amplitude ε of the forcing (cf. §4.1) is defined as $\varepsilon = \varepsilon_r |\tilde{H}(\alpha)|$, where ε_r is the roughness height. The receptivity coefficient for roughness-induced steady crossflow instability is then

$$C_R = \frac{A_{CF}}{\varepsilon_r |\tilde{H}(\alpha_{CF})|}, \tag{4.8}$$
 where A_{CF} is the receptivity amplitude of the excited crossflow vortex at the

where A_{CF} is the receptivity amplitude of the excited crossflow vortex at the roughness site. Note that (4.8) can be derived in the FRNT framework when the roughness model (4.7) is used (see e.g. Choudhari 1994, for indirect receptivity to roughness and sound).

4.2.2. Receptivity to vertical vorticity at a leading edge

Figure 4.4 is a close-up of the leading edge region of the flow configuration depicted in figure 2.7. A steady free-stream vortical disturbance in the form of a spanwise sinusoidal distribution of the streamwise velocity is considered. This particular disturbance is characterized by a vertical vorticity vector, i.e. the streamwise and spanwise vorticity components are zero. When the disturbance impinges onto the leading edge, a spanwise velocity disturbance ('crossflow') is produced (figure 2.7, plane I). Downstream of the leading edge (plane II), we

 $^{^2}$ Conditions for which the shape independence becomes invalid are discussed in paper 1.

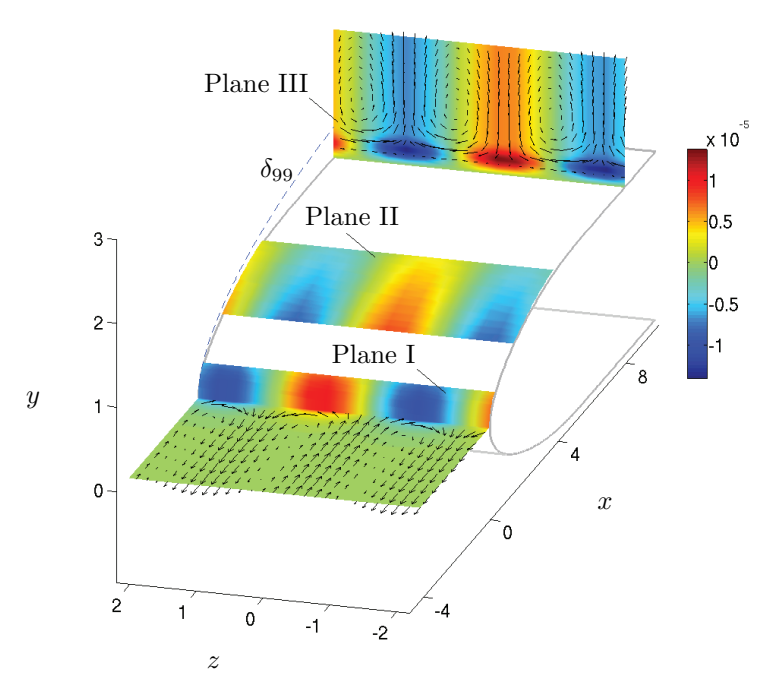


FIGURE 4.4. Instantaneous boundary-layer response to a single free-stream vortical mode with vertical vorticity only. The leading edge with aspect ratio AR=6 is considered. Plane I: colors, spanwise disturbance velocity; vectors, streamwise and spanwise disturbance. Plane II: vertical disturbance velocity ($\times 5$). Plane III: colors, streamwise disturbance velocity; vectors, vertical and spanwise components.

also identify a weak vertical velocity component. The vertical and spanwise disturbances establish a streamwise vortical motion near the boundary-layer edge. These counter-rotating vortices are able to penetrate into the boundary layer and produce streamwise disturbance streaks inside the layer (figure 2.7, plane III). The receptivity mechanism to vertical free-stream vorticity at a leading edge is summarized as follows. When impinging on the leading edge, the vertical vorticity is converted into streamwise vorticity via vortex stretching and vortex tilting. The counter-rotating streamwise vortices produce the boundarylayer streaks by the lift-up mechanism (cf. §3.5). Figure 4.5 shows boundarylayer streaks generated by this receptivity mechanism. Two leading edges with different bluntness and various spanwise wavenumbers are considered. The streak amplitudes are significantly larger when the leading edge is blunt. This suggests that the stretching and tilting of the vertical disturbance vorticity are enhanced at blunt leading edges. We conclude that boundary layers on bluff bodies are more receptive to vertical free-stream vorticity than those on slender bodies.

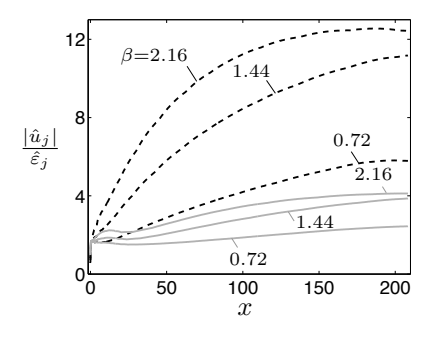


FIGURE 4.5. Downstream development of boundary-layer streaks with different spanwise wavenumbers. These streaks were initiated by the receptivity of the leading-edge flow to a free-stream disturbance with vertical vorticity only. Downstream of a blunt leading edge (AR=6, dashed lines), the streak amplitudes are larger than downstream of a slender leading edge (AR=20, solid lines).

4.2.3. Nonlinear receptivity of Görtler flow to free-stream vorticity

For low-amplitude perturbations, the receptivity mechanisms presented in §§4.2.1 and 4.2.2 are linear in the amplitude of the external forcing (roughness and vortical mode, respectively). Here, we present a nonlinear receptivity mechanism for a pair of high-frequency oblique vortical modes in the free stream over a concave plate (see §2.3.2). Figure 4.6 shows the response of the Görtler boundary layer to this kind of external forcing. A temporal-spanwise Fourier transform reveals that the flow response not only contains components with the fundamental frequency and spanwise wavenumber of the forcing, but also harmonic and subharmonic contributions (figure 4.6a). Downstream, the most energetic component is a zero-frequency disturbance with twice the spanwise wavenumber of the free-stream vorticity. This component is the Görtler roll shown in figure 3.4 and results from a nonlinear interaction between the fundamental components enforced by the free-stream disturbance. Hence, the Görtler boundary layer is receptive to high-frequency free-stream vortices, and the receptivity mechanism associated with the steady Görtler roll is nonlinear in the forcing amplitude. Figure 4.6(b) shows that the receptivity coefficient of this mechanism (defined in 4.3) decreases with increasing frequency of the free-stream disturbances.

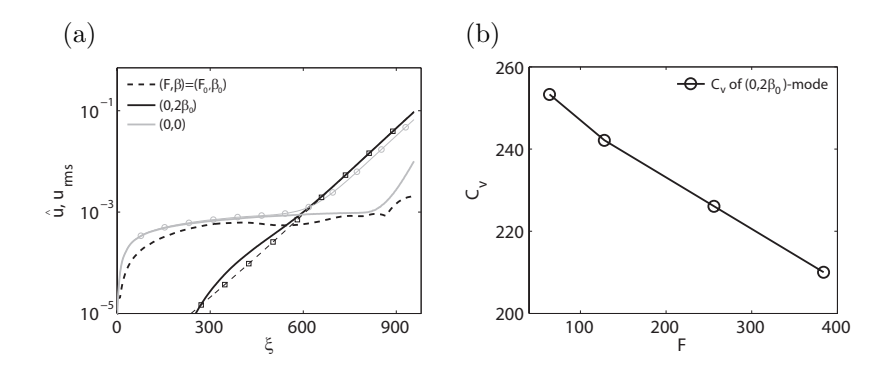


FIGURE 4.6. (a) Decomposition of the disturbance enforced inside a Görtler boundary layer by a weak pair of oblique vortical free-stream modes. Contributions with different frequencies and spanwise wavenumbers versus the tangential plate coordinate ξ . (b) Coefficient for nonlinear receptivity to oblique free-stream modes versus frequency of the external forcing.

CHAPTER 5

Breakdown

The final step of laminar-turbulent transition in boundary layers is the breakdown to turbulence, which occurs in layers with high-intensity disturbances. The breakdown is preceded by a saturation of the disturbance amplitude, indicating a nonlinear redistribution of energy to a broad range of disturbance scales (frequency/wavenumber cascade). This cascade results from nonlinear self-interactions of the fundamental disturbance and from mutual interactions between different disturbance components, promoting the emergence of harmonic and subharmonic modes, respectively. At this stage, the disturbance environment inside the boundary layer is complex, the primary disturbances in turn become unstable and a new type of instability develops on top of the flow. These new disturbances are referred to as secondary modes in order to distinguish them from the primary disturbances. It is believed that the secondary instabilities are excited by high-frequency fluctuations of the flow (e.g. free-stream turbulence). The appearance of the secondary instabilities depends on the type of boundary layer and on the kind of primary disturbance (e.g. modal/nonmodal). The secondary instabilities have, on the other hand, in common that they are three-dimensional in nature, appear as smallscale vortical structures and feature large growth rates, thus promoting a rapid breakdown of the primary instabilities. The breakdown becomes manifest in the formation of turbulent spots at random locations. These spots are patches of turbulent motion in a perturbed laminar flow (intermittent state). Since the leading edge of the turbulent spots propagates faster than the trailing edge, the spots grow in size and merge with each other. This leads to a fully turbulent boundary layer downstream.

5.1. Examples of secondary instability and breakdown

5.1.1. Streak instability in flat-plate flows

Figure 5.1 shows quasi-steady low-momentum and high-momentum streamwise disturbance streaks in a flat-plate boundary layer. These streaks were extracted from a DNS of zero pressure-gradient flow with a turbulent free stream (cf. Brandt et al. 2004; Schlatter et al. 2008). Upon saturation, the streaks strongly deform the underlying baseflow, producing inflectional wall-normal and spanwise profiles of the streamwise velocity. At this stage, the low-speed streaks become susceptive to secondary instabilities, which may become manifest in a spanwise meandering of the streaks (figure 5.1a). This type

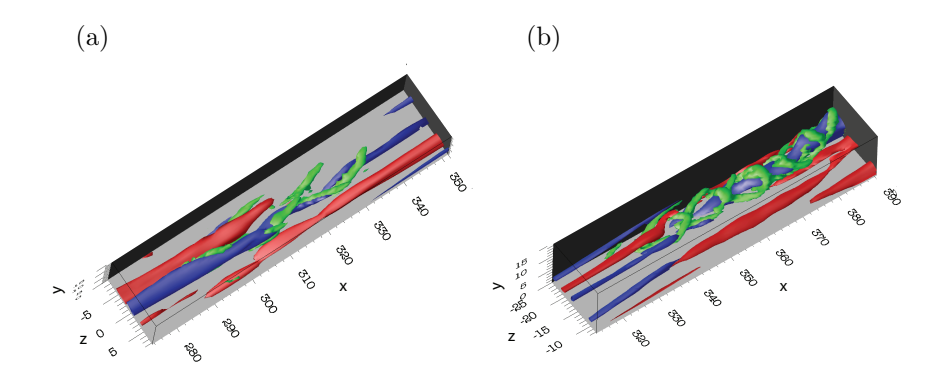


FIGURE 5.1. Secondary instabilities of low-speed streaks in a flatplate boundary layer as obtained from DNS (Brandt *et al.* 2004). (a) Sinuous and (b) varicose streak breakdown. Isocontours of streamwise disturbance velocities (blue, u = -0.15; red, u = 0.15) and of the λ_2 vortex criterion (green, $\lambda_2 = -2 \times 10^{-3}$). The flow is from lower left to upper right (reproduced after Schlatter *et al.* 2008).

of secondary motion appears as quasi-streamwise vortices at the flanks of the low-speed streaks. Because of the odd symmetry of the meandering, the instability is termed sinuous mode. Brandt $et\ al.\ (2004)$ also identified a second type of instability, manifested as a train of horseshoe-shaped vortices (figure 5.1b). The underlying streak oscillations are symmetric about the streak axis; therefore, this secondary instability is referred to as varicose mode. The sinuous and varicose streak instabilities are closely related with the odd and even modes predicted by secondary instability theory (Li & Malik 1995). These modes were demonstrated to occur near the inflection points of the spanwise (z) and wall-normal (y) flow profiles. Therefore, Li & Malik (1995) denoted the odd (sinuous) modes by 'z type' and the even (varicose) modes by 'y type'. Brandt $et\ al.\ (2004)$ found that the sinuous mode occurred more frequently in their DNS data than the varicose type.

5.1.2. Secondary instability of Görtler rolls

Figure 5.2 depicts the disturbances occurring in a Görtler boundary layer exposed to free-stream turbulence. The layer develops strong streamwise vortices and a pattern of streaklike flow structures with positive and negative streamwise disturbance velocities. The vortices and streaks constitute the steady Görtler modes described in §3.3.2. Farther downstream, small-scale vortical structures emerge on the low-speed streaks. These are the secondary instabilities initiating the breakdown to turbulence. Thus, the breakdown scenario in Görtler boundary layers is that of a streak breakdown – as in flat-plate boundary layers; however, the nature of the primary streaks is different (modal versus nonmodal). Figure 5.2 also shows that the secondary motions of the low-speed streaks are similar to those seen in figure 5.1 for the flat-plate boundary layer.

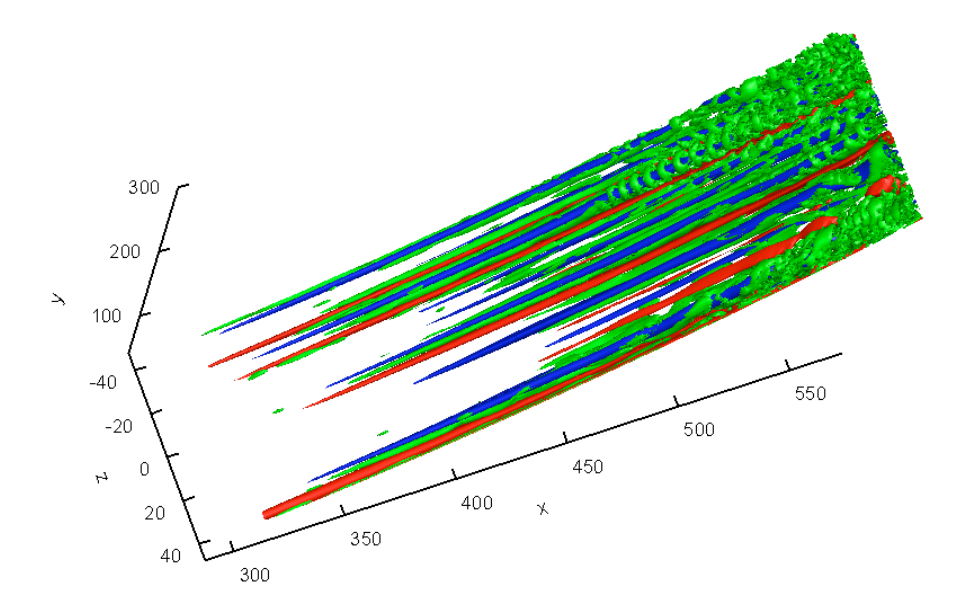


FIGURE 5.2. Disturbance structures in the transitional region of a Görtler boundary layer subject to free-stream turbulence (from DNS). Isosurfaces of streamwise disturbance velocities (blue, u=-0.25; red, u=0.2) and of the λ_2 vortex-identification criterion (green, $\lambda_2=-5\times 10^{-4}$). The flow is from left to right.

In particular, a distinct horseshoe-vortex train is prominent in figure 5.2, indicating a varicose streak breakdown. The low-speed streak at z=30, in contrast, features the spanwise meandering due to quasi-streamwise vortices typical of a sinuous secondary instability. The downstream region of the boundary layer is characterized by spanwise alternating patches of laminar and turbulent flow (intermittency), which highlights the local nature of the breakdown to turbulence.

5.1.3. Turbulent spots in swept-plate flows

We now consider the swept-plate boundary layer described in §2.3.1. Figure 5.3 depicts the boundary-layer disturbance structures excited by free-stream turbulence. The primary disturbances consist of traveling crossflow waves with different frequencies, spanwise wavelengths and amplitudes ('wave packets'). After saturating, these waves become susceptive to secondary instability modes. Malik et al. (1999) performed a secondary instability analysis of saturated crossflow vortices and identified 'z modes' and 'y modes' in analogy to those discussed in §5.1.1. Wassermann & Kloker (2003) investigated in detail the secondary instabilities of traveling crossflow waves, using DNS. The most unstable secondary mode was found near the wall and corresponded to the 'z

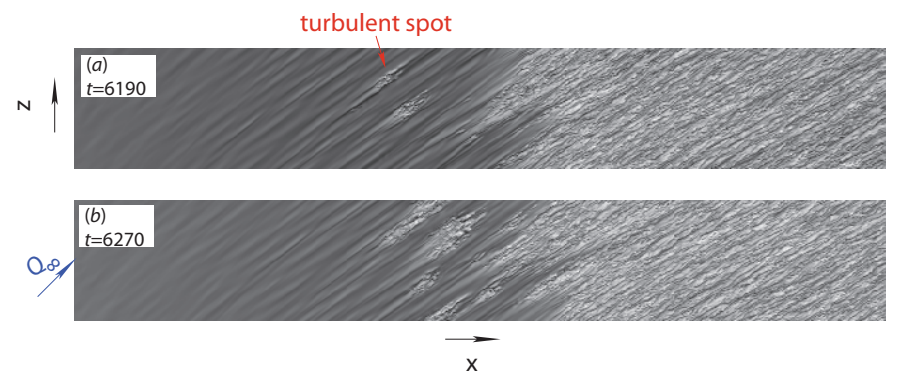


FIGURE 5.3. Turbulent spots in a swept-plate boundary layer with traveling crossflow vortices. The boundary-layer disturbances were excited by free-stream turbulence. (a) and (b) are snapshots at two times of a plate-parallel plane inside the boundary layer (y=2), showing the instantaneous chordwise disturbance velocity.

type'. However, Wassermann & Kloker (2003) conjectured that the 'y mode' might be more relevant in boundary layers exposed to turbulent free streams because it appeared near the layer edge. Figure 5.3 shows that the secondary instabilities trigger a rapid breakdown of the traveling crossflow waves to localized turbulent spots. These spots grow in size while propagating downstream (figure 5.3b) and finally merge with the fully turbulent flow.

CHAPTER 6

Numerical methods

6.1. Direct numerical simulation

Most results presented in this thesis were obtained by spatial direct numerical simulations (DNS). DNS is a numerical technique, by which the governing equations are solved directly. Terms of the Navier-Stokes equations are neither omitted (as in the PSE) nor modeled (as in the RANS equations). However, some modeling is introduced in the DNS framework by the treatment of the boundaries. These boundaries arise due to a truncation of the flow domain. An example is the modeling of (statistically) spanwise invariant flows by periodic boundary conditions. The assumption of periodicity at the spanwise boundaries introduces a fundamental spanwise wavelength (the width of the domain), which must be chosen such that it does not interfere with the physically relevant length scales of the flow.

The DNS approach requires a resolution of all dynamically important flow structures. This is an easy task for a low Reynolds-number laminar boundary layer. However, since the ratio between the largest and the smallest flow structures is proportional to $Re^{3/4}$ (length-scale cascade), the spatial resolution demands for a three-dimensional DNS increase as $Re^{9/4}$ (Moin & Kim 1997)¹. Moreover, an increase in spatial resolution requires – for methods with explicit time advancement – a reduction of the time step in order not to violate the CFL condition of numerical stability. Kim et al. (1987) and Spalart (1988) give recommendations for the maximum allowed grid spacings for DNS of wall-bounded turbulent flows. These are $\Delta x^+ = 15$, $\Delta y^+ = 1$ at the wall and $\Delta z^+ = 8$ in the streamwise, vertical and spanwise directions, respectively. The symbol '+' denotes a normalization by ν/u_{τ} ('wall units'), where $u_{\tau} = \sqrt{\tau_w/\rho}$ is the friction velocity. Most simulations reported in this thesis consider pre-transitional laminar boundary layers, characterized by larger flow structures than those in turbulent layers. The grid spacings of these DNS can therefore be chosen larger than the values given above². On the other hand, we also present simulations of transition to turbulence in a swept-plate boundary layer. In the chordwise

¹This scaling holds for DNS of homogeneous isotropic turbulence. The increase in grid points is usually less for DNS of boundary layers, because only the resolution of the layer – but not that of the free stream – needs to be refined.

²This holds, in particular, for DNS of linear receptivity and instability by a spectral method for the solution of the linearized Navier-Stokes equations, allowing for a significant reduction of the spanwise resolution.

and spanwise directions, the grid spacings of these simulations fulfilled the recommendations cited above, whereas the smallest wall-normal grid spacing was somewhat larger than $\Delta y^+=1$. Therefore, while being small enough to capture the flow structures in the pre-transitional boundary layer, the vertical grid spacing was insufficient in order to resolve the smallest scales of the fully turbulent flow. This lack of resolution was compensated for by using an LES subgrid model. The model mimicked the influence of the unresolved fluctuations on the smallest turbulent motions resolved, while being inactive in the laminar region of the boundary layer. This example shows that simulations may be considered DNS in certain regions of the flow field, whereas other regions are under-resolved, requiring a model.

We summarize that the DNS technique allows for high-fidelity simulations including all relevant length and time scales of a flow. On the other hand, the price to pay is that of long simulation times. In recent years, DNS has become more affordable thanks to the advent of supercomputers and parallelized simulation codes.

6.2. Simulation codes

The results in this thesis were obtained by using the simulation codes Simson and Nek5000. Simson uses a global spectral method (GSM) and is documented in Chevalier et al. (2007). The time-dependent incompressible Navier-Stokes equations are implemented in the velocity-vorticity formulation, where the wallnormal components of the velocity and the vorticity are the dependent flow variables. The wall-parallel velocity components are retrieved using the continuity equation and the definition of wall-normal vorticity. The spatial discretization of the governing equations builds on Fourier expansions in the wall-parallel directions and a Chebyshev expansion in the wall-normal direction. The use of Chebyshev polynomials is beneficial for simulations of wall-bounded flows, because the associated weight functions naturally concentrate the wall-normal resolution towards the wall. The use of Fourier modes requires spatially periodic solutions. Periodicity can often be assumed in the spanwise direction (spanwise invariant flows); however, boundary-layer flows are not streamwise invariant. The required streamwise periodicity must be artificially imposed by a 'fringe region' at the downstream end of the computational domain, in which the flow is forced towards the inflow conditions (Bertolotti et al. 1992)³.

The terms of the governing equations are evaluated in Fourier-Chebyshev spectral space except for the nonlinear terms, which are computed in physical space ('pseudo-spectral' treatment). This involves products between expansion coefficients, with the products at highest order (N, say) effectively leading to an expansion up to order 2N. If the number of collocation points is only equal to N, the numerical quadrature is not exact and introduces aliasing errors. For incompressible flows, these can be removed by using $\geq 3N/2$ collocation points $(3/2\text{-rule}, \operatorname{Spalart}\ et\ al.\ 1991)$. The time advancement of Simson is based on

³See also paper 1

a combined implicit-explicit scheme. The linear terms of the Navier-Stokes equations are discretized in time by a second-order implicit Crank-Nicolson scheme, whereas the nonlinear terms are discretized explicitly, using a third-order four-step Runge-Kutta scheme.

The global nature of the GSM becomes manifest in the use of global basis functions in the expansions, i.e. these functions are defined on the entire numerical domain. The major benefit of the GSM is the exponential convergence of the approximated solution, as the number of grid nodes is increased. The major shortcoming is the inability to deal with complex flow geometries and discontinuities of the flow field, e.g. shock waves.

Nek5000 is an implementation of the spectral element method (SEM) by Patera (1984) and is documented in (see Tufo & Fischer 1999; Fischer et al. 2008). The flow domain is decomposed into spectral elements, which in turn are subdivided by arrays of spectral interpolation nodes. Thus, the decomposition is both in a spatial and a spectral sense. Therefore, the SEM is sometimes classified as a method in between finite element methods and global spectral methods. The SEM is based on the weak statement of the incompressible Navier-Stokes equations, obtained by multiplying the terms of the equations by test functions and integrating over the physical domain. In particular, the viscous terms are integrated by parts, which leads to a reduction of the order of the derivatives in the viscous terms from two to one. The spatial discretization uses a Galerkin projection onto a subspace spanned by orthogonal polynomial functions. These are Lagrangian interpolants defined on Gauss-Lobatto-Legendre (GLL) nodes for the velocity space and Gauss-Legendre (GL) nodes for the pressure space, using Legendre polynomials. The interpolation is performed on GLL/GL reference elements; therefore, the linear combination of the basis functions must be mapped onto the actual elements of the flow domain in order to retrieve the expansions for the velocity and the pressure. The use of different subspaces for the velocity and the pressure is similar to the strategy of staggered grids in finite difference and finite volume methods. The aim is to avoid spurious pressure fluctuations. In Nek5000, the so-called \mathbb{P}_N - \mathbb{P}_{N-2} discretization by Maday & Patera (1989) is used. As indicated by this notation, the highest order of the polynomials used for the pressure expansion is by two lower than that for the velocity expansions. As in the GSM, the evaluation of the nonlinear terms leads to aliasing errors. These are removed by 'over-integration' similar to the 3/2-rule of fully spectral methods. Moreover, a filtering technique is implemented in Nek5000 (Fischer & Mullen 2001), allowing for a damping of the highest-order modes included in the expansions. The filtering procedure was developed in order to ensure numerical stability for simulations of high-Reynolds number turbulent flows. The discretization in time follows the implicit-explicit operator-splitting method by Maday et al. (1990). The viscous terms are treated implicitly, using a third-order backward-difference scheme, while the nonlinear terms are discretized explicitly by a second-order extrapolation.

40 6. NUMERICAL METHODS

The local nature of the SEM is manifested by the spatial decomposition into spectral elements. This allows – together with the spectral intra-elemental discretization – for two refinement strategies, based on decreasing the size of the elements ('h refinement') and on raising the highest order of the polynomials included in the expansions ('p refinement'). The major benefit of the SEM arises from its local nature, allowing for its application to flows of complex geometry; the major shortcoming is the large computational cost. In order to compensate for this, Nek5000 was designed for an efficient use on supercomputers with thousands of processors (Tufo & Fischer 2001).

6.3. Comparison

Table 6.1 gives a comparison between the GSM code Simson and the SEM code Nek5000 in order to highlight their applicability and limitations. We summarize that the GSM is – due to its efficiency – the preferred tool whenever the geometry of the simulation domain can be kept simple, allowing for a representation of the flow field in terms of a linear combination of Fourier modes. For complex geometries or flow fields with local steep gradients, requiring localized refinement, the SEM is an accurate alternative to finite difference or finite volume methods. Also note that the SEM passes into a GSM, if the physical domain of interest is decomposed into one single element only.

Table 6.1. Global spectral method (GSM) versus spectral element method (SEM).

	GSM	SEM
Simulation code	Simson	Nek5000
Programming language	Mainly Fortran77	Mainly Fortran77
General characteristics	Global approach Fourier-Galerkin- Chebyshev tau method Fast Fourier transforms	Local approach Galerkin method
Special fea- tures	Fringe technique	
Numerical grid	Equidistant in the horizontal directions, Gauss-Lobatto-Chebyshev nodes in the vertical direction	Sub-domains (spectral elements) with arbitrary shape, Gauss-Lobatto-Legendre points, staggered grids
Basis functions/ spatial discretization	Fourier modes in the horizontal directions, Chebyshev polynomials in the vertical direction	Polynomial interpolation of Lagrange form at Legendre nodes
De-aliasing	3/2-rule in the horizontal directions	Filtering at the highest wavenumbers, over- integration
Time integration	Implicit/explicit splitting: Four-step third order Runge- Kutta method + second-order Crank-Nicolson	Implicit/explicit splitting technique: Third-order backward differentiation + third-order Adams- Bashforth
Parallelisation	MPI and OpenMP Partitioning into slices in the spanwise direction	MPI Element-wise partitioning
Applications	Incompressible laminar and turbulent flows: Channel flow, 2D and 3D boundary- layer flows on flat plates	Massively parallelized simulations of incompressible laminar and turbulent flows in complex geometries
Limitations	To problems which can be made periodic using the fringe technique Simple geometries, e.g. no curved walls or leading edge	Less efficient than the global spectral method

CHAPTER 7

Summary and outlook

The present thesis reports results on the receptivity and instability of spatially evolving boundary layers to wall roughness and free-stream vortices. The results have been obtained by direct numerical simulations (DNS), using two different spectral methods. Various boundary-layer flows are considered; these are a three-dimensional boundary layer of Falkner-Skan-Cooke type, a Görtler boundary layer, a two-dimensional boundary-layer flow past a flat plate with elliptic leading edge and a swept-wing boundary layer. These flows accommodate various characteristics of the flows over straight and swept wings and blades such as the stagnation and attachment at the leading edge, wall curvature, chordwise pressure gradients, streamline curvature and crossflow.

The focus is on the receptivity of these boundary layers. The receptivity describes the coupling between the boundary-layer instabilities and the perturbations from the surroundings of the boundary layer. A receptivity analysis explains, by which mechanisms boundary-layer disturbances are produced and how large the initial amplitudes of these disturbances are. The boundary-layer receptivity must be considered in order to predict the transition location in boundary layers. Different receptivity mechanisms such as direct and indirect receptivity and linear and nonlinear receptivity are herein discussed. These mechanisms are characterized in terms of receptivity coefficients, which are a measure for the coupling efficiency between ambient perturbations and boundary-layer instabilities. Once these receptivity coefficients are known, the streamwise evolution of the amplitudes of the boundary-layer instabilities can be predicted, using linear or nonlinear methods (e.g. the PSE method).

The present thesis also reports the linear and nonlinear phases of instability growth and the breakdown to turbulence. The spatial DNS presented here are ideally suited in order to identify the relevant flow structures in spatially developing boundary layers. The value of data from spectral DNS lies in the accuracy and the completeness of the results; the drawback, on the other hand, is the tremendous computational cost. To date, DNS cannot be used to produce huge databases of receptivity coefficients for different flow parameters of interest for aeronautical engineers (e.g. Reynolds number or Mach number). Instead, simplified and more efficient methods such as the PSE and the FRNT must be addressed. These methods must, however, be verified and validated with the help of experiments or DNS. A successful validation of the PSE is, for instance, presented in Högberg & Henningson (1998) and Tempelmann et al. (2010).

In the near future, the study of swept-wing flows will be extended in order to determine the receptivity of the wing boundary layer to vortical free-stream modes and free-stream turbulence. We will also consider different representations of surface roughness (both meshed and modeled) and compute the associated receptivity coefficients. In particular, we will identify the performance of the standard linear roughness model based on inhomogeneous disturbance boundary conditions by a comparison with the results for a meshed roughness element. PSE calculations will also be considered. The aim is to combine the DNS and the PSE methods by prescribing mean-flow and disturbance profiles obtained by DNS as the upstream ('initial') condition for the PSE marching procedure. DNS is thus only used where needed (e.g. in the leading-edge region), and the PSE is employed to computed the downstream evolution of the disturbance input from the DNS.

In the far future, the optimization and flow-control techniques developed at KTH Mechanics will be applied to some of the flow configurations discussed in this thesis. Optimization techniques in hydrodynamics aim to identify the upstream flow structures causing the largest downstream disturbance amplitudes inside the boundary layer ('worst-case scenario'). These techniques have been successfully applied to relatively simple flows such as the Blasius boundary layer (Monokrousos $et\ al.\ 2010a$) and the Falkner-Skan-Cooke boundary layer (Tempelmann $et\ al.\ 2010$). Research is currently underway in order to extend the optimization analysis to the flat plate with an elliptic leading edge presented in this thesis.

The objective of flow control is to manipulate the flow by passive or active methods such that a certain objective (e.g. the delay of transition or the enhancement of mixing) is achieved. This is, for instance, accomplished by inserting actuators into the boundary layer (e.g. suction holes or active dimples). Flow-control techniques devise optimal strategies in order to achieve the objective chosen with the least possible amount of energy for the operation of the actuators. The concepts of flow control were demonstrated in two-dimensional Blasius flow (Bagheri et al. 2009), and they were recently extended to a three-dimensional configuration of the flat-plate boundary layer (Semeraro et al. 2010). These methods still await their application, for example, to the swept-wing flow considered in this thesis in order to control the amplitudes of more complicated instabilities such as crossflow vortices. Finally, the concepts of flow control need to be tested by wind-tunnel and in-flight experiments. A comparison between experimental and numerical results on flow control in a flat-plate boundary layer is given by Monokrousos et al. (2010b). A setup for wind-tunnel experiments in swept boundary layers is available at KTH Mechanics (Kurian 2010) and may be used for experimental flow control of crossflow vortices.

Acknowledgements

The present thesis reflects the outcome of about four and a half years of research within the VR¹ project 'Receptivity'. Moreover, it also reflects my – the author's – personal development throughout these years at KTH Mechanics. Both my research and personal progress were strongly influenced by my supervisors, Luca Brandt and Dan Henningson.

Luca, although you acted for the first time as a principle PhD supervisor, you guided me through my studies in the best possible manner. I was fortunate to have you as my boss and advisor. Your vast knowledge and experience are certainly impressive, but your way of dealing with students, of encouraging them, impressed me even more. Your recipe is your sense of humor. To learn from you and work with you was enjoyable.

Dan, although I had quit another PhD project before, you accepted me as your student – I am grateful for the confidence you had in me. During our biweekly research meetings, I learnt a lot from you. Your generosity shall also be highlighted here: You gave me the opportunity of attending a number of conferences, workshops and training courses within the Linné Flow Centre. I highly benefited from all these experiences.

Key to my well-being at KTH Mechanics were my wonderful colleagues – creators of an enjoyable working atmosphere. All of you were helpful, open-minded and behaved like true friends². Here, I shall devote a one-liner to those of you who were my longtime fellows and companions:

Shervin – the brilliant. My valued office mate of four and a half years. Espen – the social. Although you left the department two years ago, you are still constantly cited. Antonios – the charmer. The master of conversation, the owner of charisma and of the secret of coffee brewing. David – the perfect. The one I discussed most with and learnt most from (apart from my supervisors). Qiang – the modest. You were often able to surprise me with an unexpected joke. Johan (Ohlsson) – the rare³. You taught me how to deal with Nek5000 and the Swedes. Johan (Malm) – the busy. "You have a lot of work to do"⁴.

¹Vetenskapsrådet – The Swedish Research Council

 $^{^2\}mathrm{As}$ opposed to Facebook friends

³The only true Swede of our PhD group, potentially with Viking blood

⁴Bogusławski, L. 2010 Public communication. EFMC-8, Bad Reichenhall, Germany

You will manage. Onofrio – the aesthete. The connoisseur of classic music and owner of a fine taste. Lailai – the efficient. I enjoyed your jokes – did you like mine? Philipp – the instructive. Is there anyone giving more comprehensible seminars than you? Yohann – the maître du savoir-vivre. The master of combining outstanding research with a sense of humor, music, food and wine. Milos – the eloquent. If there is anything to explain, you will find the most appropriate words to explain it. Ardeshir – the hilarious. Laughing is healthy, you are healthier.

I also want to thank my former colleagues – those who left soon after my arrival and those who only stayed for a short while. These are Astrid, Ori, Olaf, Mathias, Jérôme, Martin, Carl-Gustav and Robin⁵. Good luck to our freshmen, Sasan and Reza. Thanks to Subir and Tobias, the two MSc students I was in charge of together with Luca. Catherine Mavriplis is acknowledged for her help with Nek5000. The people from the other KTH Mechanics groups not to be forgotten are Andreas, Amin, Enrico, Andreas, Zeinab, Florian, Peter, Tobias and Geert. I shall also thank the staff of the lab at Teknikringen 8, most notably Thomas, Bengt, Outi, Ramis, Gabriele, Jens, Fredrik, Nils and Henrik. I am also grateful to the non-academics at KTH Mechanics, in particular to Nina, Carolina, Heide, Bubba and Pär.

In 2009, I spent six months in Tamer Zaki's research group at Imperial College, London. I am indebted to Tamer, the master of efficiency and multitasking, who shared his knowledge and experience with me. I shall not forget to thank Sandeep, my best friend in London. I made extensive use of your DVAMO strategy⁶.

This thesis was proofread by Fredrik Lundell, David Tempelmann and Onofrio Semeraro, who gave valuable hints for its improvement.

Finally, the Swedish taxpayers are acknowledged. The research project was funded by VR. The simulations were carried out using SNIC computing facilities at PDC (KTH Stockholm), NSC (Linköpings universitet) and HPC2N (Umeå universitet). Moreover, resources of ICT (Imperial College London) were used for parts of the computations.

 $^{^5}$ Possibly the last KTH Mechanics thesis for you to be acknowledged

⁶Declare Victory And Move On

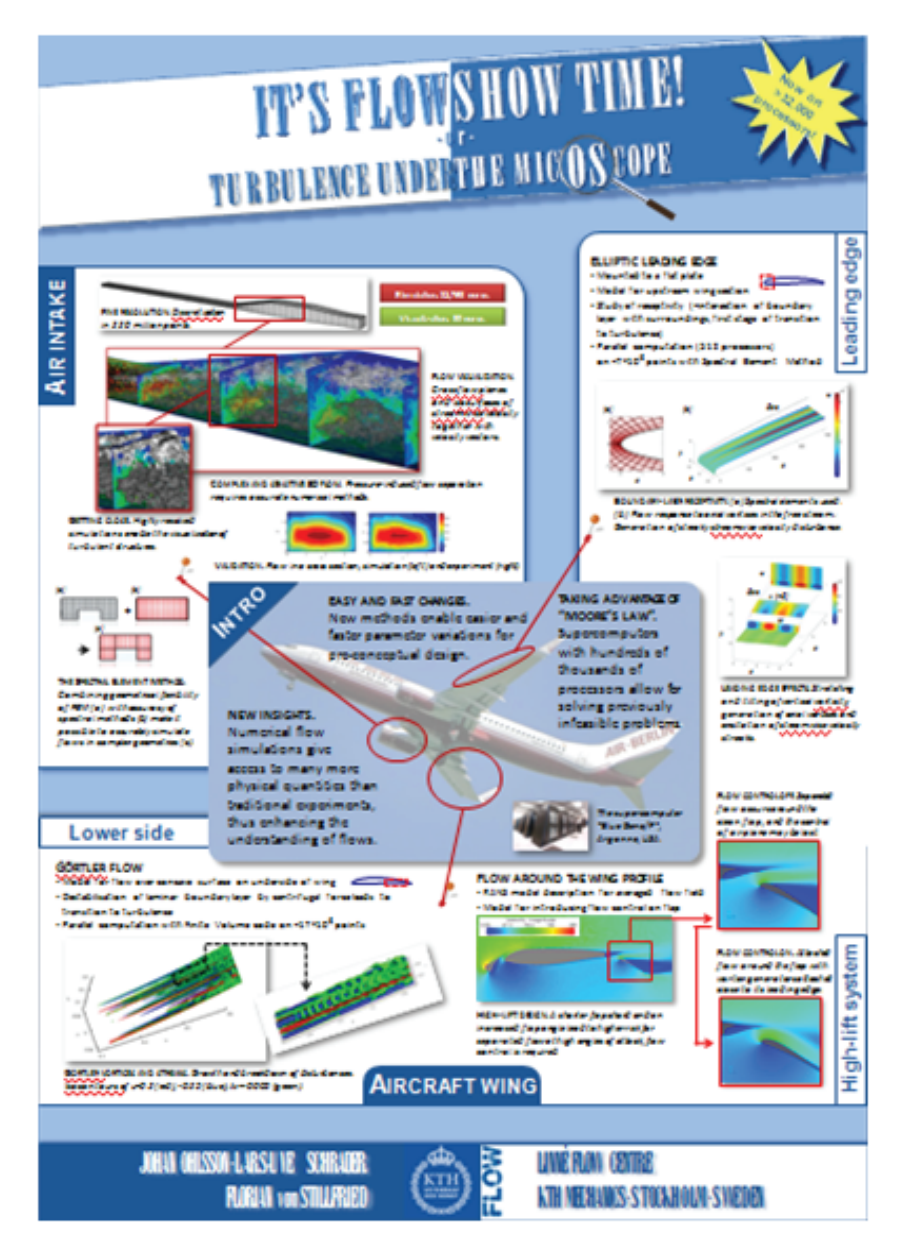


FIGURE 7.1. This poster was prepared by Johan Malm (aka Ohlsson), Florian von Stillfried and the author as a contribution to the Linné Flow Centre poster competition in January 2010. The poster did not convince the jury who preferred the competitors' more traditional contributions. Isn't it an eye-catcher anyway?

Bibliography

- Bagheri, S., Brandt, L. & Henningson, D. S. 2009 Input-output analysis, model reduction and control of the flat-plate boundary layer. *J. Fluid Mech.* **620**, 263–298.
- Bertolotti, F. P., Herbert, T. & Spalart, P. R. 1992 Linear and nonlinear stability of the Blasius boundary layer. J. Fluid Mech. 242, 441–474.
- Brandt, L., Schlatter, P. & Henningson, D. S. 2004 Transition in boundary layers subject to free-stream turbulence. *J. Fluid Mech.* **517**, 167–198.
- Butler, K. M. & Farrell, B. F. 1992 Three-dimensional optimal perturbations in viscous shear flow. *Phys. Fluids A* 4, 1637–1650.
- CHEVALIER, M., SCHLATTER, P., LUNDBLADH, A. & HENNINGSON, D. S. 2007 A Pseudo-Spectral Solver for Incompressible Boundary Layer Flows. *Tech. Rep* TRITA-MEK 2007:07. Royal Institute of Technology (KTH), Dept. of Mechanics, Stockholm.
- Choudhari, M. 1994 Roughness-induced Generation of Crossflow Vortices in Three-Dimensional Boundary Layers. *Theoret. Comput. Fluid Dynamics* 6, 1–30.
- CHOUDHARI, M. & STREETT, C. L. 1992 A finite Reynolds number approach for the prediction of boundary layer receptivity in localized regions. *Phys. Fluids A* 4, 2495–2514.
- COOKE, J. C. 1950 The boundary layer of a class of infinite yawed cylinders. In Proc. Camb. Phil. Soc., , vol. 46, pp. 645–648.
- CROUCH, J. D. 1992 Localized receptivity of boundary layers. *Phys. Fluids A* 4 (7), 1408–1414.
- CROUCH, J. D. 1993 Receptivity of three-dimensional boundary layers. AIAA Paper (93-0074).
- CROUCH, J. D. 1994 Distributed excitation of Tollmien-Schlichting waves by vortical free-stream disturbances. *Phys. Fluids* 6 (1), 217–223.
- ELLINGSEN, T. & PALM, E. 1975 Stability of linear flow. Phys. Fluids 18, 487-488.
- Falkner, V. M. & Skan, S. W. 1931 Solutions of the boundary layer equation ${f 12},$ 865–896.
- FISCHER, P., KRUSE, J., MULLEN, J., TUFO, H., LOTTES, J. & KERKE-MEIER, S. 2008 NEK5000 Open Source Spectral Element CFD solver. Https://nek5000.mcs.anl.gov/index.php/MainPage.
- FISCHER, P. F. & MULLEN, J. 2001 Filter-based stabilization of spectral element methods. C. R. Acad. Sci. Paris t. 332, Série I, 265–270.

- FJØRTOFT, R. 1950 Application of integral theorems in deriving criteria of instability for laminar flows and for the baroclinic circular vortex. *Geofys. Publ.*, *Oslo* 17 (6), 1–52.
- FLORYAN, J. M. & SARIC, W. S. 1982 Stability of Görtler vortices in boundary layers. AIAA Journal 20 (3), 316–324.
- GOLDSTEIN, M. E. 1983 The evolution of Tollmien-Schlichting waves near a leading edge. J. Fluid Mech. 127, 59–81.
- GOLDSTEIN, M. E. 1985 Scattering of acoustic waves into Tollmien-Schlichting waves by small streamwise variations in surface geometry. J. Fluid Mech. 154, 509–529.
- GÖRTLER, H. 1941 Instabilität laminarer Grenzschichten an konkaven Wänden gegenüber gewissen dreidimensionalen Störungen. ZAMM 21, 250–252, in German.
- HALL, P. 1983 The linear development of Görtler vortices in growing boundary layers. J. Fluid Mech. 130, 41–58.
- Henningson, D. S. & Åkervik, E. 2008 The use of global modes to understand transition and perform flow control. *Phys. Fluids* **20** (031302).
- HERBERT, T. 1997 Parabolized stability equations. Annu. Rev. Fluid Mech. 29, 245–283
- HERBERT, T. & BERTOLOTTI, F. P. 1987 Stability analysis of nonparallel boundary layers. Bull. Am. Phys. Soc. 32, 2079.
- HÖGBERG, M. & HENNINGSON, D. S. 1998 Secondary instability of cross-flow vortices in Falkner-Skan-Cooke boundary layers. J. Fluid Mech. 368, 339–357.
- HULTGREN, L. S. & GUSTAVSSON, L. H. 1981 Algebraic growth of disturbances in a laminar boundary layer. *Phys. Fluids* **24**, 1000–1004.
- Kim, J., Moin, P. & Moser, R. D. 1987 Turbulence statistics in fully developed channel flow at low Reynolds number. *J. Fluid Mech.* 177, 133–166.
- Klebanoff, P. S. 1971 Effect of free-stream turbulence on the laminar boundary layer. *Bull. Am. Phys. Soc.* **10**, 1323.
- Kurian, T. 2010 An experimental investigation of disturbance growth in boundary layer flows. *Tech. Rep* TRITA-MEK 2010:04. KTH Royal Institute of Technology, Department of Mechanics, Linné Flow Centre, Stockholm, Sweden.
- Landahl, M. T. 1980 A note on an algebraic instability of inviscid parallel shear flows. *J. Fluid Mech.* **98, part 2**, 243–251.
- Li, F. & Malik, M. R. 1995 Fundamental and subharmonic secondary instabilities of Görtler vortices. *J. Fluid Mech.* **297**, 77–100.
- LIN, C. C. 1955 The Theory of Hydrodynamic Stability. Cambridge University Press.
- Lin, N., Reed, H. & Saric, W. 1992 Effect of leading edge geometry on boundary-layer receptivity to freestream sound. In *Instability, Transition and Turbulence* (ed. M. Hussaini, A. Kumar & C. Streett). Springer.
- Mack, C. J., Schmid, P. J. & Sesterhenn, J. L. 2008 Global stability of swept flow around a parabolic body: connecting attachment-line and crossflow modes. *J. Fluid. Mech.* **611**, 205–214.
- Maday, Y. & Patera, A. T. 1989 Spectral element methods for the Navier-Stokes equations. In *State of the Art Surveys in Computational Mechanics* (ed. A. K. Noor), pp. 71–143. ASME, New York.
- Maday, Y., Patera, A. T. & Ronquist, E. M. 1990 An operator-integration-factor

- splitting method for time-dependent problems: Application to incompressible fluid flow. J. Sci. Comput. 5(4), 310–337.
- MALIK, M. R., LI, F., CHOUDHARI, M. M. & CHANG, C.-L. 1999 Secondary instability of crossflow vortices and swept-wing boundary-layer transition. J. Fluid Mech. 399, 85–115.
- Moin, P. & Kim, J. 1997 Tackling Turbulence with Supercomputers. Sci. American pp. 62–68.
- Monokrousos, A., Åkervik, E., Brandt, L. & Henningson, D. S. 2010a Global optimal disturbances in the blasius boundary-layer flow using time-steppers. *J. Fluid Mech.* **650**, 181–214.
- MONOKROUSOS, A., LUNDELL, F. & BRANDT, L. 2010b Feedback control of boundary layer bypass transition: Comparison of a numerical study with experiments. *AIAA Journal* **48** (8), 1848–1851.
- ORR, W. M. F. 1907 The stability or instability of the steady motions of a perfect liquid and of a viscous liquid. Part I: A perfect liquid. Part II: A viscous liquid. In *Proc. Roy. Irish Acad. A*, , vol. 27, pp. 9–138.
- Patera, A. T. 1984 A Spectral Element Method for Fluid Dynamics: Laminar Flow in a Channel Expansion. *J. Comp. Phys.* **54**, 468–488.
- PRANDTL, L. 1905 Über Flüssigkeitsbewegung bei sehr kleiner Reibung. In Verhandlungen des dritten internationalen Mathematiker-Kongresses in Heidelberg 1904 (ed. A. Krazer), pp. 484–491. Teubner, Leipzig.
- RAYLEIGH, J. W. S. 1880 On the stability, or instability, of certain fluid motions. *Proc. Lond. Math. Soc.* **11**, 57–70.
- RAYLEIGH, J. W. S. 1916 On the dynamics of revolving fluids. *Proc. Roy. Soc. Lond.* A 93, 148–154.
- Reddy, S. C. & Henningson, D. S. 1993 Energy growth in viscous channel flows. J. Fluid Mech. 252, 209–238.
- Reynolds, O. 1883 On the experimental investigation of the circumstances which determine whether the motion of water shall be direct or sinuous, and the law of resistance in parallel channels. *Phil. Trans. R. Soc. Lond. Mech.* 174, 935–982.
- RUBAN, A. I. 1985 On the generation of Tollmien-Schlichting waves by sound. Fluid Dynamics 19, 709–716, translated from Izvestiya Akademii Nauk SSSR, Mekhanika Zhidkosti i Gaza, No. 5, pp. 44–52, 1984.
- SARIC, W. S. 1994 Görtler vortices. Annu. Rev. Fluid Mech. 26, 379-409.
- Schlatter, P., Brandt, L., delange, H. C. & Henningson, D. S. 2008 On streak breakdown in bypass transition. *Phys. Fluids* **20** (101505), invited paper.
- Schmid, P. J. & Henningson, D. S. 2001 Stability and Transition in Shear Flows. Springer.
- Schubauer, G. B. & Skramstad, H. K. 1947 Laminar boundary layer oscillations and stability of laminar flow. *J. Aero. Sci.* 14, 69–78.
- Semeraro, O., Bagheri, S., Brandt, L. & Henningson, D. S. 2010 Feedback control of three-dimensional optimal disturbances using reduced-order models. *J. Fluid Mech.* Submitted.
- Somers, D. M. & Horstmann, K.-H. 1985 Design of a Medium-Speed, Natural-Laminar-Flow Airfoil for Commuter Aircraft Applications. *Tech. Rep* IB 129-85/26. Deutsches Zentrum für Luft- und Raumfahrt (DLR).
- SOMMERFELD, A. 1908 Ein Beitrag zur hydrodynamischen Erklärung der turbulenten

- Flüssigkeitsbewegungen. In Proc.~4th~Internat.~Congr.~Math., , vol. III, pp. 116–124. Rome.
- Spalart, P. R. 1988 Direct simulation of a turbulent boundary layer up to Re $_{\theta}$ =1410. J. Fluid Mech. 187, 61–98.
- SPALART, P. R., MOSER, R. D. & ROGERS, M. M. 1991 Spectral methods for the Navier-Stokes equations with one infinite and two periodic directions. J. Comp. Phys. 96, 297–324.
- SQUIRE, H. B. 1933 On the stability of three-dimensional disturbances of viscous flow between parallel walls. In Proc. Roy. Soc. Lond. A, , vol. 142, pp. 621–628.
- Taylor, G. I. 1939 Some recent developments in the study of turbulence. In *Proc.* 5th Intl. Congr. Appl. Mech. (ed. J. P. D. Hartog & H. Peters), pp. 294–310. Wiley.
- Tempelmann, D., Hanifi, A. & Henningson, D. S. 2010 Spatial optimal growth in three-dimensional boundary layers. *J. Fluid Mech.* **646**, 5–37.
- Theofilis, V., Barkley, D. & Sherwin, S. 2002 Spectral/hp element technology for global flow instability and control. *Aeronaut. J.* **106**, 619–625.
- Trefethen, L. N., Trefethen, A. N., Reddy, S. C. & Driscoll, T. A. 1993 Hydrodynamic stability without eigenvalues. *Science* **261**, 578–584.
- Tufo, H. M. & Fischer, P. F. 1999 Terascale spectral element algorithms and implementations. In *Supercomputing*, *ACM/IEEE 1999 Conference*. Portland, USA.
- Tufo, H. M. & Fischer, P. F. 2001 Fast Parallel Direct Solvers for Coarse Grid Problems. J. Parallel Distrib. Comput. 61 (2), 151–177.
- Wassermann, P. & Kloker, M. 2003 Transition mechanisms induced by travelling crossflow vortices in a three-dimensional boundary layer. *J. Fluid Mech.* 483, 67–89.
- Zavol'skii, N. A., Reutov, V. P. & Rybushkina, G. V. 1983 Generation of Tollmien-Schlichting waves via scattering of acoustic and vortex perturbations in boundary layer on wavy surface. *J. Appl. Mech. Tech. Phys.* **24 (3)**, 355–361, translated from Zhurnal Prikladnoi Mekhaniki i Tekhnicheskoi Fiziki, No. 3, pp. 79–86, 1983.